AGU PUBLICATIONS

Tectonics

RESEARCH ARTICLE
10.1002/2015TC003913

Key Points:
- New (U-Th)/He and published thermochronometric data were modeled using Pecube
- Models quantified age, rates, and magnitude of Southern Snake Range extension
- Extension initiated in the Eocene, and continued in the Oligocene and Miocene

Supporting Information:
- Text S1, Figure S1, and Captions of Tables S1 and S2
- Table S1
- Table S2

Correspondence to:
S. L. Evans,
evanss3@unlv.nevada.edu

Citation:
Evans, S. L., R. H. Styron, M. C. van Soest, K. V. Hodges, and A. D. Hanson (2015), Zircon and apatite (U-Th)/He evidence for Paleogene and Neogene extension in the Southern Snake Range, Nevada, USA, *Tectonics*, *34*, 2142–2164, doi:10.1002/2015TC003913.

Received 27 APR 2015
Accepted 11 SEP 2015
Accepted article online 14 SEP 2015
Published online 15 OCT 2015

Zircon and apatite (U-Th)/He evidence for Paleogene and Neogene extension in the Southern Snake Range, Nevada, USA

Sarah L. Evans[1], Richard H. Styron[2], Matthijs C. van Soest[3], Kip V. Hodges[3], and Andrew D. Hanson[1]

[1]Department of Geoscience, University of Nevada, Las Vegas, Nevada, USA, [2]Earth Analysis, Seattle, Washington, USA, [3]School of Earth and Space Exploration, Arizona State University, Tempe, Arizona, USA

Abstract Despite decades of study, the timing, rates, and magnitude of extension in the Basin and Range are poorly quantified in some areas. This study integrates new zircon and apatite (U-Th)/He analyses (ZrnHe and ApHe) with published thermochronologic data to quantify these extensional parameters in the Southern Snake Range (SSR) of east-central Nevada. The new ZrnHe dates range from 40.7 ± 4.9 Ma in the western SSR to 21.0 ± 3.3 Ma near the present-day trace of the Southern Snake Range Décollement (SSRD), and the ApHe dates range from 15.1 ± 2.4 Ma in the central SSR to 13.6 ± 0.7 Ma closest to the SSRD trace. These new and previously published low-temperature thermochronologic cooling ages were inverted for the extensional history of the SSR using a Bayesian Monte Carlo method incorporating Pecube. The posterior extensional histories indicate three significant pulses of extension occurred during the Paleogene and Neogene: (1) ~50–45 to ~38 Ma (Eocene), (2) ~33–30 to ~23 Ma (Oligocene), and (3) ~23–20 to ~10–8 Ma (Miocene). Modeled rates of extension were low at ≤ 0.5 mm a^{-1}; however, more rapid rates possibly occurred during the Eocene and the Miocene based on posterior histories. Net cumulative extension from posterior histories is 19.8 to 34.9 km, with a mean of 29.7 km. About 10–18 km of extension occurred during the Eocene and Oligocene. Model results indicate no relationship between extension and magmatism in the SSR. Our new model results and interpretations also indicate extensional collapse of the Nevadaplano initiated prior to ~17 Ma.

1. Introduction

Over the past several decades, geologic research has focused on the structural history (e.g., the style, timing, rates, and magnitude of extension) of the Basin and Range of western North America. In particular, metamorphic core complexes (MCC) have been a focus of intense study because these features have accommodated large-magnitude extension [e.g., *Coney and Harms*, 1984; *Buck*, 1991; *Wernicke*, 1992]. Determining the structural history of MCC is particularly important for understanding large-scale driving mechanisms for extension within the subprovinces of the Basin and Range [e.g., *Sonder and Jones*, 1999]. However, despite intense study of MCC in the Northern Basin and Range (NBR) during the past several decades [e.g., *Armstrong*, 1972; *Allmendinger et al.*, 1983; *Miller et al.*, 1983; *Bartley and Wernicke*, 1984; *Dallmeyer et al.*, 1986; *Wells et al.*, 1990; *Hodges and Walker*, 1992; *MacCready et al.*, 1997; *Wells et al.*, 2000; *Colgan and Henry*, 2009; *Konstantinou et al.*, 2012] the structural history has not been strictly quantified throughout the Cenozoic for some of these important features. In the Southern Snake Range (SSR), part of the Snake Range MCC (Figure 1a), the structural history is only partially understood for the Southern Snake Range Décollement (SSRD), the main structure responsible for extension in the range [e.g., *Miller et al.*, 1999].

Quantifying the structural history (e.g., timing, magnitude, and rates of extension) for the partially understood SSRD provides new evidence that may be used to address important issues about the extensional history of the NBR. Some models for the evolution of the NBR suggest that there are regional links between magmatism and extension [e.g., *Gans et al.*, 1989; *Best and Christiansen*, 1991; *Axen et al.*, 1993; *Best et al.*, 2013], and the validity of these proposed models can be addressed at the scale of the SSR once the extensional history is better understood. Hypothesized relationships between the Snake Range MCC and other extensional structures of the region [e.g., *Taylor*, 1990; *Taylor and Bartley*, 1992; *Axen et al.*, 1993] may also be tested with information about the extensional history. Additionally, the timing of the collapse of the Nevadaplano may be inferred for this portion of the NBR given quantitative values for the onset and magnitude of extension in the SSR, as previously completed in other regions [e.g., *Colgan and Henry*, 2009]. To constrain these

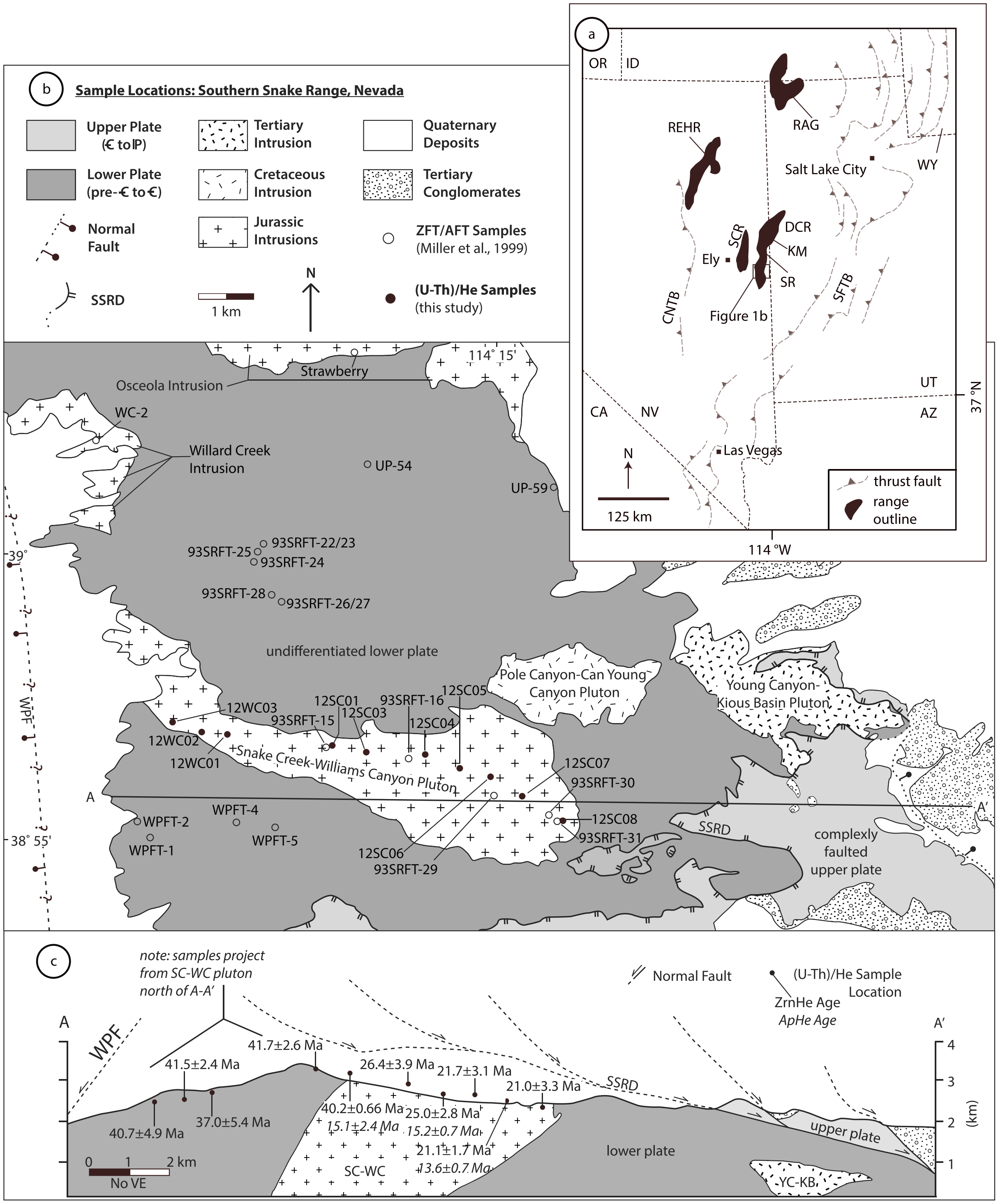

Figure 1. (a) Location of the Snake Range in east-central Nevada between the Central Nevada thrust belt (CNTB) of *Taylor et al*. [2000] and the Sevier fold and thrust belt (SFTB) [e.g., *DeCelles and Coogan*, 2006] (modified from *Miller and Gans* [1989], *DeCelles and Coogan* [2006], and *Long* [2012]). Dashed lines indicate generalized thrust faults, teeth on hanging walls. Dashed and dotted lines are state outlines. Black polygons are generalized range outlines. (b) Simplified geologic map of the central Southern Snake Range showing the location of (U-Th)/He samples (this study) and fission track samples of *Miller et al*. [1999] (map modified from *Whitebread* [1969], *McGrew* [1993], and *Miller et al*. [1999]). Names for intrusions are from *Lee and Christiansen* [1983] and *McGrew* [1993]. (c) Generalized cross section of *McGrew* [1993] for the central Southern Snake Range with (U-Th)/He dates projected into the line of section. Abbreviations: REHR = Ruby Mountain-East Humboldt Range, RAG = Raft River-Albion-Grouse Creek Range, SR = Snake Range, OR = Oregon, ID = Idaho, WY = Wyoming, UT = Utah, AZ = Arizona, NV = Nevada, and CA = California, SSRD = Southern Snake Range Décollement, WPF = Wheeler Peak Fault, SC-WC = Snake Creek-Williams Canyon Pluton, YC-KB = Young Canyon-Kious Basin Pluton, ZrnHe = zircon (U-Th)/He age, ApHe = apatite (U-Th)/He age, VE = vertical exaggeration.

important extensional parameters and address these issues, new thermochronologic data, zircon and apatite (U-Th)/He analyses (ZrnHe and ApHe), were determined for the SSR. These new data were integrated with previously reported zircon and apatite fission track ages (ZrnFT and ApFT) [*Miller et al*., 1999] by modeling the data using the software package Pecube [*Braun*, 2003; *Braun et al*., 2012] and methods modified from *Styron et al*. [2013]. *Styron et al*. [2013] defined a methodology for using the Pecube software package to model timing, magnitude, and rates of extension in a Tibetan MCC. Those methods are refined into a more efficient Bayesian inversion for a multistage extensional history, as well as thermal parameters (radiogenic heat production and Moho temperature) that control thermochronometric cooling ages.

The integrated thermochronologic data and modeling allows us to address several important research questions regarding the extensional history of the SSR, such as the following: (1) Did the majority of extension in the SSR occur during a Miocene period of extension along the Snake Range-Deep Creek fault system as proposed by *Miller et al*. [1999]? (2) Are there additional periods of extension in the SSR, similar to those documented in the Eocene and Oligocene in the better studied Northern Snake Range (NSR) [e.g., *Lee*, 1995]? (3) What is the magnitude of extension in the SSR and how does it compare to previous estimates by *McGrew* [1993] and *Miller et al*. [1999]? (4) Is there evidence for pre-Cenozoic extension in the SSR as documented in the upper crust of the NBR west of the SSR [e.g., *Druschke et al*., 2009; *Long et al*., 2015]? And (5) does our understanding of temporal relationships between extension and magmatism, relationships to other regionally important structures, and timing of Nevadaplano collapse need to be revised in light of these new data?

2. Regional Geologic Setting

The tectonic history of east-central Nevada extends to at least the late Proterozoic, when Neoproterozoic to Devonian strata were deposited in the passive margin of western North America following the breakup of Rodinia [e.g., *Dickinson*, 2006]. Passive margin sedimentation in the region ceased in the Late Devonian with the onset of the Antler Orogeny [e.g., *Poole et al*., 1992; *Dickinson*, 2006]. Late Devonian to Pennsylvanian strata of east-central Nevada were deposited in basins associated with the Antler orogeny (e.g., Antler foreland basin) and other late Paleozoic deformation [e.g., *Trexler et al*., 2004]. The overall thickness of Neoproterozoic to Permian strata in the NSR is estimated at ~10 to 12 km [*Miller et al*., 1983], and between 10 and 15 km regionally [*Miller et al*., 1992].

During the Jurassic to Cretaceous this area of east-central Nevada experienced several episodes of plutonic intrusion, metamorphism, and large-scale folding [e.g., *Miller et al*., 1988; *Dickinson*, 2006]. Several Jurassic aged plutons are exposed in the SSR, NSR, and possibly in the Schell Creek Range (SCR) [*Lee and Christiansen*, 1983; *Miller et al*., 1988]. Jurassic metamorphism reached amphibolite grade in the SSR and was associated with the intrusion of the Snake Creek-Williams Canyon (SC-WC) pluton [*Miller et al*., 1988; *McGrew*, 1993] at ~160 Ma [*Lee and Christiansen*, 1983]. East-central Nevada was also intruded by several plutons during the Cretaceous between 110 and 75 Ma [*Miller et al*., 1988]. The SSR also experienced minor metamorphism around the time of emplacement of a two-mica granite, the Pole Canyon-Can Young Canyon pluton [*Miller et al*., 1988; *McGrew*, 1993] at ~79.1 to 79.7 Ma [*Lee et al*., 1970, 1986; *Miller et al*., 1988]. Penetrative metamorphism in the Cretaceous occurred in the NSR [*Miller et al*., 1988; *Lewis et al*., 1999; *Cooper et al*., 2010], SCR, Deep Creek Range, and Kern Mountains [*Miller et al*., 1988]. Based on thermobarometic studies, the footwall of the Northern Snake Range Décollement (NSRD) was buried to depths of 25–30 km [*Lewis et al*., 1999; *Cooper et al*., 2010] during Cretaceous metamorphism at ~88 Ma [*Cooper et al*., 2010]. No thermobarometric studies have been completed in the footwall of the SSRD to ascertain depths of burial prior to Cenozoic extension.

East-central Nevada occupied a hinterland position during the Sevier orogeny [e.g., *DeCelles and Coogan*, 2006]. During the Sevier event, this part of the hinterland was uncut by thrusts based on several studies of the sub-Tertiary/Oligocene unconformity [e.g., *Armstrong*, 1972; *Miller et al*., 1983; *Long*, 2012], leading several authors to conclude that the Sevier hinterland prior to the Tertiary was a thick, elevated orogenic plateau [e.g., *Coney and Harms*, 1984; *DeCelles*, 2004]. This "Nevadaplano" [*DeCelles*, 2004] was located between the Central Nevada thrust belt to the west [*Taylor et al*., 2000] and the Sevier fold and thrust belt to the east [*Coney and Harms*, 1984; *DeCelles and Coogan*, 2006]. Its elevation may have been ≥2 km in the Late Cretaceous based on a clumped stable isotope study of carbonates from eastern Nevada and central Utah

[*Snell et al*., 2014]. Although this region was not involved in thrusting during the Sevier orogeny, some areas underwent synconvergent extension. This phenomenon is well documented by the onset of midcrustal extension in the Cretaceous in the Raft River-Albion-Grouse Creek MCC [*Wells et al*., 1990] and Ruby-East Humboldt MCC [*Hodges and Walker*, 1992] and by the onset of surface-breaking normal faulting in the Egan Range of east-central Nevada [*Druschke et al*., 2009] and in the Eureka Culmination of central Nevada [*Long et al*., 2015].

Following the Sevier orogeny, east-central Nevadan crust was highly attenuated and experienced minor plutonism and voluminous volcanism during the Cenozoic [e.g., *Coney and Harms*, 1984; *Gans*, 1987; *Miller et al*., 1988; *Dickinson*, 2006]. Crustal thicknesses of ~50 km in the Sevier hinterland were thinned to present-day thicknesses of ~30–35 km during Cenozoic extension in the NBR [*Gans*, 1987]. Extension in the NBR occurred on both high-angle faults and on low-angle detachments [e.g., *Miller et al*., 1983; *Bartley and Wernicke*, 1984; *Gans*, 1987; *Miller et al*., 1999].

Multiple periods of extension of varying intensity have been proposed for the Snake Range and the associated Deep Creek Range and Kern Mountains fault systems [*Armstrong*, 1972; *Miller et al*., 1983; *Lee*, 1995; *Miller et al*., 1999]. *Lee* [1995] proposed three discrete extensional events at 48–41 Ma, 30–26 Ma, and 20–16 Ma in the NSR using ^{40}Ar/^{39}Ar multiple diffusion domain (MDD) modeling of potassium feldspars. A rapid period of extension in the Miocene around 17 Ma was documented in the NSR, SSR, SCR, Deep Creek Range, and in the Kern Mountains based on ZrnFT and ApFT data [*Miller et al*., 1999]. Quaternary to present day extension on high-angle range bounding faults in east-central Nevada has also been documented [e.g., *Dohrenwend et al*., 1996; *Wesnousky and Willoughby*, 2003; *U.S. Geological Survey and Nevada Bureau of Mines and Geology*, 2006; *DePolo*, 2008], and a geodetic study documented modern day “distributed extension” from east-central Nevada to west-central Utah [*Kreemer et al*., 2010].

3. Snake Range Geologic Setting

The NSR is a Cordilleran MCC with a ductilely deformed and mylonitized lower plate in contact with a brittlely extended upper plate along a detachment surface [e.g., *Miller et al*., 1983; *Coney and Harms*, 1984]. Geologic investigations of the NSR have established a detailed tectonic evolution of the core complex based on mapping, structural analyses, interpretations of geophysical data, thermobarometric, and thermochronologic studies [e.g., *Allmendinger et al*., 1983; *Miller et al*., 1983; *Bartley and Wernicke*, 1984; *Gans et al*., 1985; *Lee and Sutter*, 1991; *Lee*, 1995; *Lewis et al*., 1999; *Miller et al*., 1999; *Cooper et al*., 2010]. The Cenozoic evolution of the SSR and SSRD has been less intensively studied [e.g., *Armstrong*, 1972; *McGrew*, 1993; *Miller et al*., 1999], possibly because the SSRD was not initially recognized as structurally linked to the NSRD [e.g., *Miller et al*., 1983]. Nevertheless, the SSRD accommodated a significant amount of extension during the Cenozoic [e.g., *McGrew*, 1993; *Miller et al*., 1999], and a systematic study of the timing and rates of extension is necessary to fully understand extension in the NBR.

3.1. Extensional History of the SSRD

The SSRD is currently a low-angle structure that is exposed throughout the SSR [e.g., *Whitebread*, 1969] (Figure 1b). The SSRD separates metamorphosed Neoproterozoic to Cambrian strata and Mesozoic and Paleogene intrusions in the lower plate [*Lee and Christiansen*, 1983; *Miller et al*., 1988] from unmetamorphosed Cambrian to Permian strata in the upper plate [*Whitebread*, 1969; *McGrew*, 1993]. Additionally, the upper plate of the SSRD contains a variety of Cenozoic volcanic and minor sedimentary deposits [*Whitebread*, 1969; *McGrew*, 1993; *Miller et al*., 1999]. Although, the SSRD was originally interpreted as a thrust fault [e.g., *Drewes*, 1958; *Misch*, 1960], it was subsequently recognized as a Tertiary extensional feature [*Armstrong*, 1972] and as part of the extensive (~150 km along strike) Miocene Snake Range-Deep Creek fault system [*Miller et al*., 1999].

The exact timing of extension along the SSRD is unclear. Cataclasis and mylonitization of a ~36 Ma pluton [*Miller et al*., 1988] in the SSR suggests that extension occurred post-intrusion [*McGrew*, 1993]. Pre-Oligocene extension may be recorded by ~40–42 Ma ZrnFT ages from the lower plate of SSRD and a pre-31 Ma conglomerate in the upper plate of the SSRD, but the exact timing, amount, and rate of extension prior to the Oligocene is not understood [*Miller et al*., 1999]. *Lee et al*. [1970] interpreted K-Ar ages from the SSR to indicate movement on the SSRD between ~17 and 18 Ma but attributed these ages to thrusting along the SSRD rather than extension. *Miller et al*. [1988] reinterpreted these K-Ar ages to be the result of intrusion of the Young

Canyon-Kious Basin pluton at ~36 Ma and hydrothermal alteration. Finally, a fission track study interpreted extension in the SSR to have occurred along high-angle normal faults sometime before 31 Ma, based on the ZrnFT data and a pre-31 Ma conglomerate, and again at ~17 Ma, based on ApFT data [*Miller et al*., 1999]. This Miocene extension was interpreted to have been "rapid," though no formal slip rate was defined, and to have occurred along the strike of ~150 km of interconnected extensional faults in the SSR, NSR, Kern Mountains, and Deep Creek Range [*Miller et al*., 1999].

Overall extension on the SSRD has been estimated at 8 to 24 km based on a retrodeformable cross section constructed by *McGrew* [1993]. The ~17 Ma period of extension documented by the ApFT data is thought to have accommodated ~15 km of slip on the SSRD based on an assumed high-angle fault geometry and a 35°C km^{-1} geothermal gradient [*Miller et al*., 1999]. No Cenozoic slip rate has been determined for the SSRD by previous research. This study combines previously collected ApFT/ZrnFT data and new ApHe and ZrnHe data with finite element modeling to better understand the overall timing, magnitude, and rates of extension in the SSR during the Cenozoic.

4. (U-Th)/He Thermochronology

ZrnHe and ApHe thermochronology has been applied to a variety of tectonic settings to understand near-surface and upper crustal (<10 km) processes [e.g., *House et al*., 1998; *Stockli et al*., 2000; *Farley*, 2002; *Ehlers and Farley*, 2003; *Reiners*, 2005; *Stockli*, 2005; *Colgan et al*., 2006; *Flowers et al*., 2008; *Schildgen et al*., 2009a; *Colgan et al*., 2010; *van Soest et al*., 2011; *Styron et al*., 2013]. These thermochronometers can be used to determine when a sample cooled below a specific temperature (i.e., closure temperature) [*Dodson*, 1979] or temperature range (i.e., helium partial retention zone (HePRZ)) [e.g., *Wolf et al*., 1998]. The ZrnHe thermochronometer has a HePRZ of 140–200°C [*Wolfe and Stockli*, 2010], and a closure temperature that ranges from 175 to 193°C given a cooling rate of 10°C Myr^{-1} for typical grain sizes [*Reiners*, 2005]. The ApHe system has a HePRZ between ~40 and 80°C [*Wolf et al*., 1998; *House et al*., 1999; *Stockli et al*., 2000] and has a closure temperature of ~75°C [*Farley*, 2000]. Assuming a conservative geothermal gradient of 30°C km^{-1} for the NBR during the Cenozoic, the ZrnHe and ApHe thermochronometers would record exhumation of upper crustal rocks from ~6.7 to 1.3 km depth. These low-temperature thermochronometers are thus powerful tools for understanding the exhumation of lower plate rocks of MCC in the upper crust.

Ten rock samples were collected for ZrnHe and ApHe analysis from the Jurassic SC-WC intrusion [*Lee and Christiansen*, 1983] at ~1–1.5 km intervals along an almost 10 km long horizontal transect roughly parallel to the ESE slip direction of the SSRD [*McGrew*, 1993] (Figure 1b). *Stockli* [2005] outlined this sampling strategy for low-temperature thermochronometers in extensional tectonic settings to determine the magnitude of extension and fault slip rates.

4.1. (U-Th)/He Results

Mineral separation and single-grain (U-Th)/He analyses were completed in the Group 18 Laboratories (NG^{3}L) at Arizona State University using techniques similar to those described by *Schildgen et al*. [2009a, 2009b] and *van Soest et al*. [2011]. Raw zircon and apatite (U-Th)/He dates were corrected for the loss of ^{4}He in the outer ~20 μm of the mineral structure (alpha ejection correction) using standard methods from *Farley et al*. [1996], *Farley* [2002], and *Hourigan et al*. [2005]. Individual dates for 44 zircon and 11 apatite crystals are reported in Tables S1 and S2 in the supporting information with uncertainties based on analytical imprecision alone; the error-weighted mean dates for sets of zircon or apatite analyses from each sample are shown in Table 1. In many cases, the dispersion of ZrnHe or ApHe dates from a single sample exceeded the variation that might be expected given the magnitude of analytical uncertainties. As a result, for each ensemble of ZrnHe or ApHe dates of a sample, clear outliers were determined using the Hampel identifier, as described by *Pearson* [2011], assuming a threshold value of 4. Any outliers determined by this method were rejected, and the weighted mean was recalculated. Final dispersions were evaluated using mean squared weighted deviation (MSWD) [*Wendt and Carl*, 1991]. For groups of dates without excess dispersion, the uncertainties reported in Table 1 represent two standard deviations of the error-weighted mean ($2\sigma_{wm}$) based on the propagation of analytical uncertainties alone. For groups of dates with excess dispersion, the calculated $2\sigma_{wm}$ values were multiplied by the square root of the MSWD, and the result was reported as an expanded uncertainty $2\sigma_{exp}$ in an attempt to account for the scatter. The reported uncertainties do not take into account natural zoning of U and Th isotopes within the crystal lattice [e.g., *Hourigan et al*., 2005].

Table 1. (U-Th)/He Data

Sample	Latitude[a] (°N)	Longitude[a] (°W)	Elevation (m)	Age[b] (Ma)	$\pm2\sigma_{wm}$[c] (Ma)	$\pm2\sigma_{exp}$[d] (Ma)	$MSWD_{wm}$	Aliquots
				Williams Canyon (Zircon)				
12WC01	38.9474	114.3292	2710	37.0	0.61	5.4	78	3
12WC02	38.9484	114.3366	2567	41.5	0.67	2.4	12	4[e]
12WC03	38.9512	114.3449	2472	40.7	0.53	4.9	84	5
				Snake Creek (Zircon)				
12SC01	38.9444	114.2983	3316	41.7	0.60	2.6	19	4
12SC03	38.9425	114.2886	3224	40.2	0.66	0.89	1.8	4[e]
12SC04	38.9418	114.2715	2944	26.4	0.34	3.9	133	5
12SC05	38.9378	114.2614	2666	25.0	0.33	2.8	71	5
12SC06	38.9354	114.2525	2671	21.7	0.26	3.1	150	6
12SC07	38.9296	114.2431	2538	21.1	0.30	1.7	34	4
12SC08	38.9223	114.2328	2373	21.0	0.30	3.3	120	4
				Snake Creek (Apatite)				
12SC03	38.9425	114.2886	3224	15.1	0.29	2.4	66	5
12SC05	38.9378	114.2614	2666	15.2	0.38	0.7	3.5	3
12SC07	38.9296	114.2431	2538	13.6	0.38	0.7	3.1	3

[a]WGS 1984 datum.
[b]Weighted mean of aliquots not excluded by Hampel identifier.
[c]Propagated analytical error of weighted mean.
[d]Expanded error calculated by multiplying the square root of $MSWD_{wm}$ and σ_{wm}.
[e]An aliquot was excluded from weighted mean age based on the Hampel identifier.

4.1.1. Zircon (U-Th)/He Results

We obtained ZrnHe dates for all 10 rock samples. The dates range from 40.7 ± 4.9 Ma for a sample collected near the western end of the horizontal transect to 21.0 ± 3.3 Ma for a sample closest to the SSRD trace (Table 1, Figures 1c and 2). The distribution of ZrnHe dates in the SSR is bimodal, with a cluster of Eocene dates (37.0 ± 5.4 to 41.5 ± 2.4 Ma) in the western portion of the transect, and an abrupt transition to Oligocene dates (21.0 ± 3.3 to 26.4 ± 3.9 Ma) in the central to eastern portion of the transect (Figures 1c and 2). The Eocene population shows no apparent age progression from west to east. However, the Oligocene

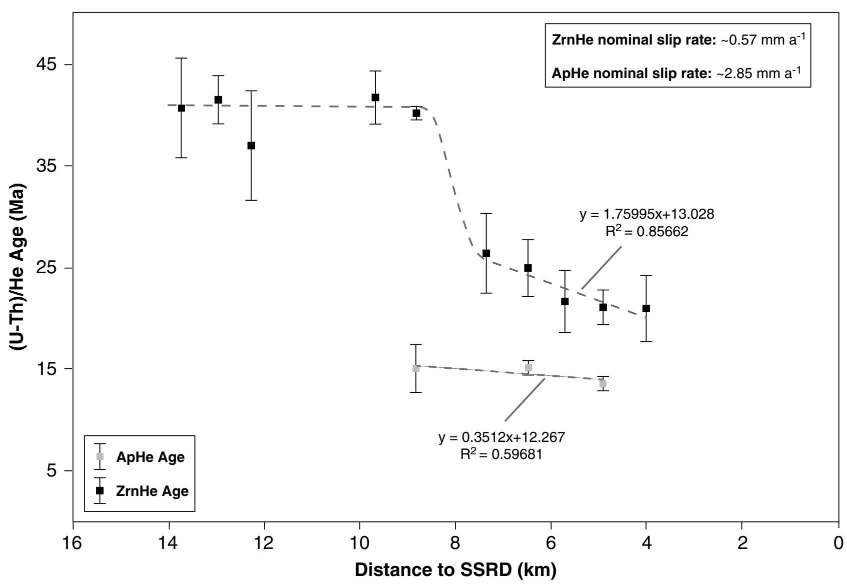

Figure 2. Plot of measured zircon and apatite (U-Th)/He ages versus distance from the SSRD. Nominal slip rates are calculated using a simple linear regression and inverse of the regression slope [e.g., *Stockli*, 2005]. Equation of linear regression and correlation coefficient are shown. Black dashed line is a visual aid for changes in ages. Age values and error bars are those quoted in Table 1. Abbreviations: ZrnHe = zircon (U-Th)/He age, ApHe = apatite (U-Th)/He age.

dates show a systematic decrease in the direction of extension, with the youngest dates coming from samples collected closest to the trace of the SSRD (Figures 1c and 2).

Nine of the 10 weighted mean dates are overdispersed as shown by greater than anticipated MSWD values [*Wendt and Carl*, 1991]. All ZrnHe dates were evaluated for correlations with effective uranium concentration (eU) to assess if radiation damage may have contributed to dispersion of replicate dates (Table S1) [e.g., *Reiners*, 2005; *Guenthner et al*., 2013]. A single aliquot 12WC02 z03 was found to have a high eU and a significantly younger date compared to the other 12WC02 replicate analyses. However, this replicate was excluded from the error-weighted mean date based on the outlier identification method (Tables 1 and S1). No other samples showed a significant range in eU values with a corresponding correlation to ZrnHe dates; as a result, radiation damage is not considered to be a major factor in the overdispersed dates. Instead, this overdispersal may be the result of parent isotope zonation within the zircon crystals, which was shown by *Hourigan et al*. [2005] to contribute to overdispersed ZrnHe dates. Although zircons with obvious optical zoning were not chosen for analysis, it was impossible to completely avoid zoned grains since nonacicular zircons in the SCWC commonly exhibit some zonation [*Lee et al*., 1968]. This is considered to be the most likely cause of the overdispersed ZrnHe dates.

4.1.2. Apatite (U-Th)/He Results

Only three samples yielded apatite grains suitable for (U-Th)/He dating (Table 1). All three were collected in the central to eastern portion of the footwall transect. ApHe dates from the three samples decrease from 15.1 ± 2.4 Ma in the central portion of the transect to 13.6 ± 0.7 Ma closest to the SSRD (Figures 1c and 2). In the western section of the transect, a previous study documented ≤ 0.02 wt % apatite present in the intrusion [*Lee et al*., 1973], and the few apatites observed contained inclusions, rendering them unfit for conventional ApHe analysis [e.g., *Wolf et al*., 1996]. Only the ApHe dates from sample 12SC03 exhibit significant overdispersion, and this is most likely due to unrecognized inclusions containing U, Th, or Sm. None of the ApHe samples showed a large range in eU values among replicate analyses (Table S2). Therefore, radiation damage is not considered to be a major factor in the overdispersed dates as observed in other ApHe date populations [e.g., *Shuster et al*., 2006; *Flowers et al*., 2009].

4.2. Thermochronologic Data Interpretation

Ranges of denudation rates were estimated for the SSR using (U-Th)/He and fission track samples that were dated by multiple thermochronometers ($n = 6$). We used these rates to assess the relative influences of erosional and tectonic denudation in the SSR. For the (U-Th)/He data, denudation rates were calculated from samples 12SC03, 12SC05, and 12SC07 (Table 1) [e.g., *Reiners and Brandon*, 2006]. The previously published ZrnFT and ApFT data for samples 93SRFT-29, 93SRFT-30, and 93SRFT-31 from *Miller et al*. [1999] were also used to estimate denudation rates in the same manner. The *Reiners and Brandon* [2006] method assumes nominal closure temperatures for each thermochronometer (ZrnFT: 240°C, ZrnHe: 180°C, ApFT: 110°C, ApHe: 65°C; 10°C Myr^{-1} cooling rate) when determining cooling rates and assumed steady state geothermal gradients to calculate denudation rates.

Minimum and maximum cooling rates were calculated for each sample based on the errors of each date. For example, 12SC03 has a minimum calculated cooling rate of 4.05°C Myr^{-1} and a maximum cooling rate of 5.27°C Myr^{-1}. Although these cooling rates are less than 10°C Myr^{-1}, as assumed for the nominal closure temperature, the ~5–6°C difference does not significantly change the closure temperature of either system for typical grain sizes [e.g., *Reiners*, 2005]. The cooling rate minimum, average, and maximum values were then divided by a range of geothermal gradients from 10 to 50°C km^{-1}. These calculations lead to an estimated minimum denudation rate of 0.08–0.4 km Myr^{-1} for sample 12SC03. This analysis was completed for all six samples, and the range of denudation rates for the SSR is 0.08–2.25 km Myr^{-1}. Two samples (12SC03 and 93SRFT-29) with Eocene ZrnHe and ZrnFT dates, closest to one another in the range, were used to calculate Eocene denudation rates between 0.15 and 6.35 km Myr^{-1}.

These calculated denudation rates are 16 to 1270 times greater than the present-day median global outcrop erosion rate of 0.005 km Myr^{-1} [*Portenga and Bierman*, 2011]. Although the median outcrop erosion rates from *Portenga and Bierman* [2011] are only calculated for the present, the significantly higher denudation rates estimated for the SSR suggest that even if erosion rates were higher in the past (e.g., during a warm Eocene climate), unreasonably higher rates would be necessary to attribute the majority of denudation in the SSR to erosional processes. As a result of this comparison, erosional denudation is assumed to be negligible, and the majority of exhumation is considered to be of tectonic origin for the SSR.

The ZrnHe and ApHe cooling ages for the SSR are progressively younger in the extension direction, as expected for exhumation along a normal fault (Figure 2) [e.g., *John and Foster*, 1993; *Wells et al.*, 2000; *Stockli*, 2005]. The observed age distribution in the central and eastern part of the transect is consistent with exhumation due to unroofing by extension along the SSRD during the Oligocene starting at ~26–25 Ma and continuing into the Miocene to at least ~13.6 Ma based on the youngest ApHe age in the transect. The mechanism for Eocene cooling of the western portion of the transect below ~140°C is less clear from these data alone. The onset of extension interpreted from the ZrnHe data is 8 to 9 Myr older than a previous estimate for movement along the SSRD from ApFT data [*Miller et al.*, 1999]. This difference in minimum age for the onset of extension is a function of the higher closure temperature of the ZrnHe system in comparison to the ApFT system.

A one-dimensional paleodepth reconstruction [e.g., *Stockli et al.*, 2003] of the available low-temperature thermochronologic data was completed using the retrodeformable cross section of *McGrew* [1993] (Figure S1). Difficulties in quantifying the errors associated with the paleodepth reconstruction, and a lack of definable age-depth relationships does not allow for direct interpretation of the timing and rates of exhumation in the SSR. Instead, to better understand the extension history of the SSR based on our new data and previously published ZrnFT and ApFT data, a Pecube [*Braun*, 2003; *Braun et al.*, 2012] modeling approach was used.

Pecube is an ideal tool to investigate the tectonothermal history of the SSR, as it is well suited to modeling multiple-sample thermochronological data sets given relatively simple deformational scenarios. In particular, the relatively time-invariant fault geometry of the SSRD at depth [*McGrew*, 1993] avoids Pecube's limitations on time-varying fault geometry. Furthermore, the nature of our data set (~30 footwall thermochronometer ages, with few samples yielding multiple ages from multiple thermochronometers) makes it more suitable for an analysis tool that exploits the spatial and structural relationships between samples to constrain the time-temperature-exhumation history of the samples, rather than a tool that emphasizes single-sample, multiple-thermochronometer analysis such as HeFTy [*Ketcham*, 2005].

5. Thermochronologic Modeling

We reconstruct the extensional history of the SSR through a Bayesian inversion incorporating the thermokinematic modeling program Pecube as well as structural estimates for total strain and fault slip [e.g., *McGrew*, 1993] using methods derived from *Styron et al.* [2013]. The inversion essentially takes random tectonothermal histories for the SSR, filters them so that they are within structural constraints (section 5.2.1), uses Pecube to predict thermochronometric ages for each history, and selects posterior histories based on the goodness of fit between the predicted and observed thermochronometer ages. This process yields joint posterior probability distributions for the thermal and tectonic variables in the inversion.

The Bayesian approach to inversion for continuous model variables is well described mathematically [e.g., *Sambridge*, 1999; *Sambridge and Mosegaard*, 2002; *Tarantola*, 2005], but here we focus on a procedural description and use mathematical descriptions as an aid rather than as the most compact description of the process. Bayesian inversion or inference involves taking initial estimates of probability distributions for each variable of interest and then refining those estimates based on how well predictions made by the variables compare to observations. The initial estimates are called "prior probabilities" or simply "priors," and the refined probabilities are known as "posterior probabilities." Whether a distribution is a prior or posterior distribution is solely based on whether it will be refined in the inversion step at hand, and in many instances the posteriors for one inversion step form the priors for another. However, in our methods this iteration does not happen.

The priors map to the posteriors through another distribution called the "likelihood," which encapsulates the goodness of fit between the model predictions and the observations. This is summarized by Bayes' rule:

$$p(T \mid D) \propto p(T)p(D \mid T) \tag{1}$$

where $p(T)$ is the prior probability distributions for all variables in T (in our case, variables that represent the thermal and strain history); $p(T \mid D)$ is the posterior probability distributions, i.e., the probability distributions of the variables T given the data D; and $p(D \mid T)$ is the likelihood, i.e., the probability of observing the data D given that the parameters T are true.

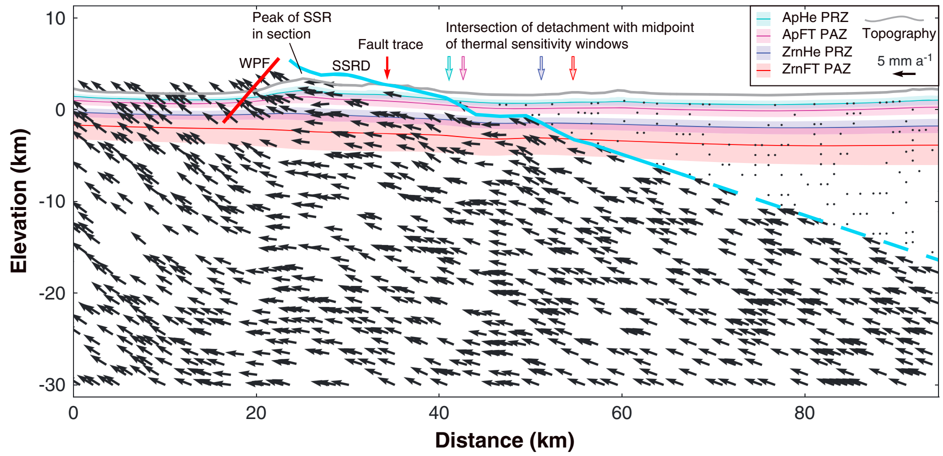

Figure 3. East-west oriented cross section example of the Pecube model setup for the SSR. The SSRD geometry in solid blue and WPF geometry in solid red are taken from the *McGrew* [1993] retrodeformable cross section. Dashed blue line is the extrapolated extension of the SSRD to the edge of the model. Vectors indicate velocity of rocks modeled relative to the stable hanging wall. The intersection of the middle of the thermal sensitivity window of each thermochronometer is indicated on the cross section. Abbreviations: SSRD = Southern Snake Range Décollement, WPF = Wheeler Peak Fault, SSR = Southern Snake Range, ApHe PRZ = apatite (U-Th)/He partial retention zone, ApFT PAZ = apatite fission track partial annealing zone, ZrnHe PRZ = zircon (U-Th)/He partial retention zone, ZrnFT PAZ = zircon fission track partial annealing zone.

5.1. Pecube Model Setup

The Pecube finite element model (FEM) covers the entirety of the SSR, with an areal distribution of 119 km E-W by 32 km N-S. The upper surface of the model is the modern topography, taken from SRTM data [*Farr et al.*, 2007]. Topographic evolution is modeled as steady state across the FEM. The model extends to 30 km depth, based on the present-day distance to the Moho in the Snake Range [*Gans*, 1987]. Node spacing in the FEM mesh is 900 m in the *x*, *y*, and *z* directions. The FEM has two faults, the SSRD and Wheeler Peak Fault (WPF) (Figure 3). The retrodeformable cross section of *McGrew* [1993] suggests that the fault geometries of the SSRD and WPF remain relatively constant throughout extension. The geometries of the faults in the subsurface for the model are taken from *McGrew* [1993]. The mineral elongation of mylonites exposed in the eastern SSR documented by *McGrew* [1993] was used to define the slip direction of the SSRD at 105° and a generalized strike for the structure at 015°. This inferred strike is similar to a generalized strike of 007° calculated based on a corrugation axis of the SSRD from mapping of *McGrew and Miller* [1995]. The Pecube software does not allow for lateral or temporal changes in fault geometry. The strike orientation of the SSRD in the east-central SSR (closest to the measured mineral elongations) must be extrapolated to the northern and southern portions of the range. As a result, the modeled trace of the SSRD farther away from the east-central portion of the range is less representative of the mapped trace of the SSRD.

Pecube uses several variables to calculate the “steady state” geothermal gradient in the FEM, which is then perturbed by tectonic deformation; variables used to define this are the temperatures at the model surface and base (the Moho in our FEM), thermal diffusivity, atmospheric lapse rate, and radiogenic heat production. We fix the FEM surface temperature, thermal diffusivity, and atmospheric lapse rate, values that are reasonably well constrained relative to the Moho temperature and radiogenic heat production. The Moho temperature and radiogenic heat production are solved in the inversion. Table 2 lists the values for all fixed parameters in the model.

5.2. Construction of Priors

The initial step in the inversion is construction of geologically reasonable priors. In order to solve for both the coupled strain history and thermal state of the crust, representative model variables were defined (Table 2).

The strain history of the SSR is separated into independent histories for the SSRD and WPF. These histories are then discretized into several time intervals with different slip rates. The time boundaries of each slip interval and the slip rates for each interval are all randomly sampled from uniform probability distributions.

Table 2. Pecube Modeling Input Parameters

Parameter	Value
Fixed Parameters	
Model dimensions (length, width)	119 km E-W and 32 km N-S
FEM node spacing (*x*, *y*, *z* directions)	900 m
Thermal diffusivity[a]	25 km^2 Myr^{-1}
Moho depth[b]	30 km (present day)
Surface temperature[c]	15°C
Atmospheric lapse rate	0°C km^{-1}
Prior Parameters[d]	
SSRD	
Generalized strike of structure	015°
Span of slip history	80–5 Ma
Slip rates	0–10 mm a^{-1}
Number of slip intervals	4
WPF	
Span of slip history	40–0 Ma
Slip rates	0–4 mm a^{-1}
Number of slip intervals	3
Thermal Parameters	
Moho temperatures	600–1100°C
Radiogenic heat production	5–50°C Ma^{-1}

[a]From *Whittington et al.* [2009].
[b]From *Gans* [1987].
[c]Global mean annual temperature.
[d]See sections 5.1 and 5.2 for discussion of values and references.

Slip on the SSRD has four intervals between 80 and 5 Ma, with the beginning and end points for the entire slip history occurring anywhere in this interval, and possible slip rates between 0 and 10 mm a^{-1} at any time. Note that successive intervals are allowed to have the same slip rate, so substantial changes in slip rate are not enforced between intervals.

Direct evidence (i.e., cross-cutting relationships) to define the boundaries for onset and completion of extension on the SSRD are poor, and previous work largely inferred the slip history of the SSRD from thermochronologic data [e.g., *Lee et al.*, 1970, 1980; *Miller et al.*, 1988, 1999]. The most direct evidence for timing of motion along the SSRD comes from the ~36 Ma Young Canyon-Kious Basin pluton [*Miller et al.*, 1988] which contains both mylonitic and cataclastic deformation features that are interpreted to be a result of motion along the SSRD [*McGrew*, 1993]. *Armstrong* [1972] also interpreted an Oligocene age of motion based on a normal fault mapped as cross-cutting Oligocene volcanics of the Needles Range Group [*Whitebread*, 1969; *Best and Grant*, 1987] that was interpreted to either merge into or was truncated by the SSRD. *Miller et al.* [1999] described fanglomerates on the eastern edge of the SSR that contain Oligocene-aged volcanic clasts and interpreted these strata as deposits directly related to extension on the SSRD after the Oligocene. Although these relationships point to an Oligocene age and younger period of extension on the SSRD they do not preclude pre-Oligocene periods of extension on the SSRD. The Eocene ZrnHe dates from the eastern portion of our transect suggest that extension may have begun prior to the Oligocene. Therefore, a maximum age for extension on the SSRD is set at 80 Ma, based on the timing of Cretaceous metamorphism recorded in the Pole Canyon-Can Young Canyon pluton at ~79.7–79.1 Ma [e.g., *Lee et al.*, 1970, 1986; *Miller et al.*, 1988; *McGrew*, 1993].

Three intervals of slip between 40 and 0 Ma were defined for the WPF. Slip rates at any time on the WPF were defined between 0 and 4 mm a^{-1}. The WPF is active, defining the lower age bound, and has a slip rate of $<$ 0.2 mm a^{-1} [*Sawyer*, 1998; *U.S. Geological Survey and Nevada Bureau of Mines and Geology*, 2006]. *McGrew* [1993] also included either this structure or a similarly oriented structure, in an intermediate stage of extension in the SSR; as a result, an intermediate age in the range for slip history of the SSRD (40 Ma) was chosen as an upper age bound. Fewer modeled intervals of slip are used for the WPF due to its shorter extensional history in comparison to the SSRD. Similar to the SSRD, these intervals allow variability within the model.

Moho temperatures were varied between 600 and 1100°C, and radiogenic heat production from 5 to 50°C Ma^{-1}. These broad ranges were chosen because these parameters are not well constrained for the SSR; however, they combine to yield upper crustal geothermal gradients of 20–55°C km^{-1}, bracketing Tertiary estimates for the Basin and Range [e.g., *Foster and John*, 1999; *Stockli et al.*, 2002; *Gorynski et al.*, 2013; *Long et al.*, 2015]. The combination of these thermal parameters with the strain history variables yields a prior distribution $p(T)$, where T is the set of probability distributions for each variable t in T. Each $p(t)$ is independent of the others.

5.2.1. Filtering of Priors to Fit Structural Constraints

When constructing $p(T)$, we chose probabilities $p(t)$ for each t that are individually reasonable (or at least possible) and considered independent. However, many combinations of the variables yield extension histories that violate constraints from geologic cross sections by producing unreasonable magnitudes of net extension. Therefore, we only considered the subset of $p(T)$ that is consistent with geological constraints, which we call

$p(T \mid G)$, or the probability of T given geological constraints G. From a practical perspective, by reducing $p(T)$ to a much smaller or much more sparse $p(T \mid G)$ before the computationally intensive Pecube modeling, the total computation times may be reduced by 1 or 2 orders of magnitude with no loss of statistical robustness, as $p(t \mid G)$ may be very similar to $p(t)$ for any t.

A very effective way to reduce $p(T)$ to $p(T \mid G)$ is to filter samples from $p(T)$ that predict net extension outside of acceptable bounds determined by geologic cross sections [e.g., *Styron et al.*, 2013]. We arithmetically calculate the net extension for each sample of $p(T)$ given fault dips from the FEM and strain history variables from the $p(T)$ sample and accept into $p(T \mid G)$ only those with net extension values between 8 and 35 km. This estimate is in part based on the 8–24 km of allowable extension from a nonunique retrodeformable cross section that assumes a specific SSRD upper plate geometry and a footwall cutoff in the Cambrian Pole Canyon Limestone [*McGrew*, 1993]. The total allowable extension was increased from 24 to 35 km, so the model would not be overly constrained by a single interpreted cross section; however, the models were not forced to a total of 35 km of extension. We iteratively sampled and filtered $p(T)$ until $p(T \mid G)$ had 9999 samples, which were then run in Pecube.

5.3. Calculating Likelihood With Pecube

We use Pecube to predict thermochronometer ages at our sample locations in order to calculate $p(D \mid T)$. Pecube models were run on the Eureka cluster at the National Supercomputing Center for Energy and the Environment at the University of Nevada, Las Vegas. Each model took between 0.5 and 2.5 h to compute. Parallelization of about 100X allowed us to run the ~15,000 CPU hours of computation in a little over a week. Out of 9999 jobs, 18 (0.2%) finished with errors, and therefore, the total number of runs considered is 9981.

We evaluate each model from $p(T \mid G)$ by calculating the relative model likelihood $p(D \mid T)$ using the equation

$$p(D \mid T) = \frac{\exp\left(-\chi^2\right)}{\exp\left(-\chi^2_{\text{min}}\right)} \tag{2}$$

where χ^2 is the goodness-of-fit statistic for normally distributed data

$$\chi^2 = \frac{1}{N}\Sigma_{i=1}^{N}\frac{\left(\mu_i - \hat{\mu}_i\right)^2}{\sigma_i^2} \tag{3}$$

μ is the error-weighted mean date, $\hat{\mu}$ is the modeled age, and σ_{wm} is the standard deviation of the weighted mean. Since the constant of proportionality in equation (1) is unknown, we normalize $p(D \mid T)$ relative to the best fitting model [*Tarantola*, 2005].

5.4. Posterior Sampling

Once the relative likelihoods were calculated for each model, we calculated the posterior $p(T \mid D)$, or “sampling the posterior” in Bayesian terminology, by selecting models from $p(T \mid G)$ proportional to their likelihood [e.g., *Mosegaard and Tarantola*, 1995]. In practice, this is done through selection of models whose likelihood is larger than a number randomly sampled from the uniform distribution [0,1). This random number is independently generated for each comparison.

5.5. Model Results

$p(T \mid D)$ contains 39 models out of 9981 considered. Figure 4 shows the observed and modeled ages plotted by longitude (a good proxy for downdip distance on the SSRD). These plots show that the model ages match measured dates within 2σ in most cases, except for three ApFT and two ZrnHe samples. It is possible that unrecognized complications in the fault geometries (e.g., corrugations and fault splays) of the SSRD and WPF were not represented in Pecube causing the modeled ages to not accurately represent measured ages. However, it is also possible that the measured values were themselves spurious results. The three ApFT samples were interpreted as only partially reset [*Miller et al.*, 1999], and the two ZrnHe samples have unacceptably high MSWD_{wm} values. Despite these misfits, overall the modeled ages and measured thermochronologic ages are generally in good agreement.

The posterior distribution $p(T \mid D)$ is the complete solution to a Bayesian inverse problem. However, because of the multivariate nature of $p(T \mid D)$, we transformed the strain variables into extensional histories in order to describe and make inferences from them (Figure 5).

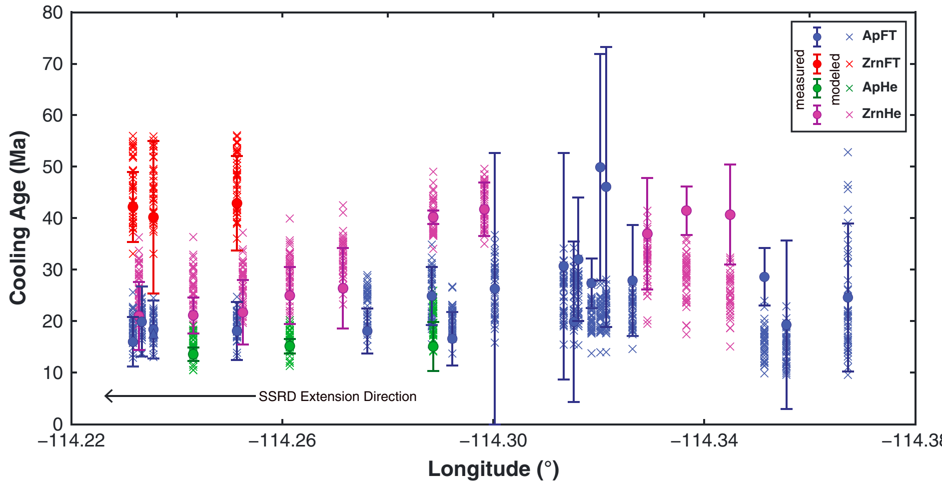

Figure 4. Plot of all measured and modeled cooling ages from the posterior distribution versus location in longitude within the SSR. Measured ages for the ZrnFT, ApFT, ZrnHe, and ApHe systems are represented by colored circles and error bars (ZrnHe and ApHe: $2\sigma_{wm}$; ZrnFT and ApFT: 2σ). Please see Table 1 for ZrnHe and ApHe values and errors and *Miller et al.* [1999] for ZrnFT and ApFT values and errors. Colored cross symbol represents the modeled cooling age for the 39 best fit models. The overall agreement between modeled ages and measured ages is relatively good. Please see section 5.5 for a discussion of the ages with poor agreement. Abbreviations: ZrnFT = zircon fission track age, ApFT = apatite fission track age, ZrnHe = zircon (U-Th)/He age, ApHe = apatite (U-Th)/He age, SSRD = Southern Snake Range Décollement.

The results indicate that extension in the SSR starts during the Eocene at ~50–45 Ma (Figures 5a and 5b). Extension rates begin to increase in the SSR at ~50 Ma (Figure 5a). However, the median and mean onsets of extension for the 39 best fit models are ~45 Ma. Cumulative extension in the SSR by the Eocene-Oligocene boundary (Figure 6a) shows a slightly bimodal distribution, with 23 of the 39 fits requiring greater than 2 km of extension prior to the Oligocene. The mean amount of extension accumulated prior to 34 Ma is 5.8 km, with a range of 0.9–9.8 km of extension over the central 50% of results (25th to 75th percentile interval; Figure 5b). Extension rates during the Eocene are generally slow at ~0.5 mm a^{-1} (Figure 5a). However, individual modeled histories show variability in the extension rate with some results showing periods of extension with rates as high as 6 mm a^{-1} (Figure 5a). Despite these low rates of extension, we regard this phase as likely responsible for producing the Eocene cooling of the higher-temperature and highest-elevation thermochronometers along the western end of the transect.

Following the inferred onset of extension in the Eocene, the model results show low extension rates from ~38 to ~33–30 Ma, where all but one modeled history show extension at rates of < 0.5 mm a^{-1} (Figure 5a). Modeled extension rates increased again in the early Oligocene and remained at levels comparable to the Eocene extension rates until the Oligocene-Miocene boundary. Although the overall rate of extension from ~50–45 to 38 Ma and from ~33–30 to 23 Ma was rather slow, it was significant enough to produce cumulative extension of ~10–18 km for most modeled histories by 23 Ma (Figure 6b). The mean cumulative extension of all model fits is 11.3 km, with a range of 6.7–15.5 km over the central 50% of modeled histories for net cumulative extension at the Oligocene-Miocene boundary. This period of extension is inferred to be responsible for the Oligocene ZrnHe cooling ages observed in the SSR.

Modeling results further suggest that the significant but relatively slow extension during the Eocene and Oligocene was followed by a period of more rapid extension during the Miocene. The most rapid extension rates occur at ~16.5 Ma (Figure 5a); however, a histogram of modeled extension rates at 16.5 Ma (Figure 6c) shows that about half of the model fits have extension rates of ≤ 1 mm a^{-1}. Some individual models show more rapid extension rates of 6 and 8 mm a^{-1}, although most do not show rates greater than 3.5 mm a^{-1}. At that time, the WPF may have begun to extend at extremely low rates (Figure 5c). This fault may have initiated as early as ~20 Ma, and the modeling results indicate extension started by ~10 Ma (Figure 5c). The modeled extension rates on the WPF increased steadily after 10 Ma but remain very low at ≤ 0.3 mm a^{-1} until present day (Figure 5c).

Overall modeled cumulative net extension in the SSR ranged from 19.8 to 34.9 km. Figure 6d shows that most results have cumulative net extension amounts at the higher end of that range. The central 50% of results

10.1002/2015TC003913

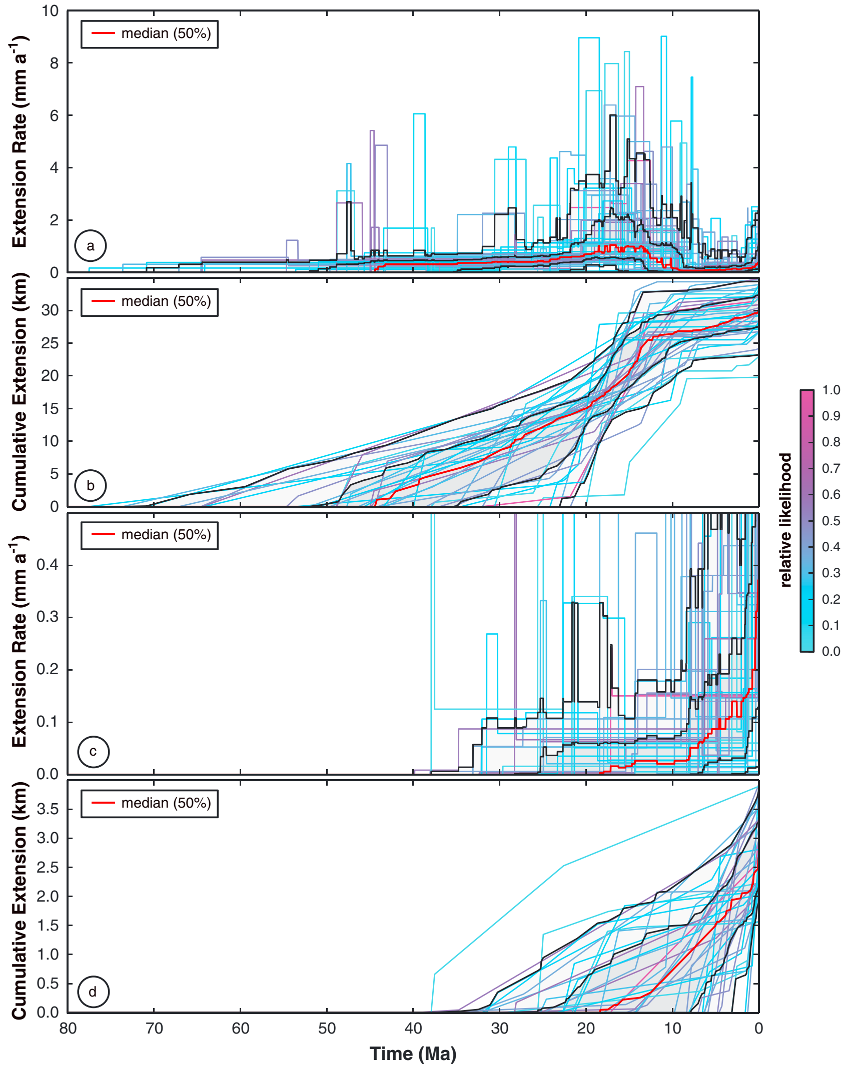

Figure 5. Extensional history (a and b) for the entire SSR and (c and d) for the WPF from 39 of 9981 runs, where each colored line represents the relative likelihood of a particular model history based on Bayesian inversion of the $p(TG)$ to produce the posterior distribution $p(T \mid D)$ (see sections 5.3 and 5.4 of text for further explanation). Purple-colored model histories are relatively more likely than blue-colored model histories. The red line represents the median extension rate and cumulative extension through time for the SSR. The dark gray shaded area represents a 25th–75th percentile bound around the median for the modeled histories. Light gray shaded area represents a 5th–95th percentile bound around the median for the modeled histories. (a) The extension rate is low on average throughout the Cenozoic in the SSR; however, individual model histories show a fair amount of variability. (b) The median onset of extension for the SSR is ~45 Ma and a median net cumulative extension of ~30 km. (c) Extension rate on the WPF is very low on average at < 0.5 mm a^{-1}. (d) The median onset for extension on the WPF is ~19 Ma; however, accumulation of extension in the system does not occur until ~10 Ma.

have a range of 27.5–32.3 km of cumulative net extension and a mean cumulative net extension of 29.7 km. The contribution of WPF to cumulative net extension is minor, with a mean extension amount of 2.8 km and a total range of 1.5–3.9 km for all modeled histories (Figure 5d).

5.6. Relationships Between Model Variables and Results

No single variable is strongly correlated with model likelihood, and therefore, no variable strongly influences the results. Additionally, the posterior variables $p(T \mid D)$ are poorly correlated, which seems to indicate that the results are essentially random. However, inspection of the results in terms of "metavariables" (i.e., combinations of input variables that better characterize the system) shows data patterns, although due to the high dimensionality of the system, some scatter still exists in many plots. This is illustrated in Figures 5 and 7. For example,

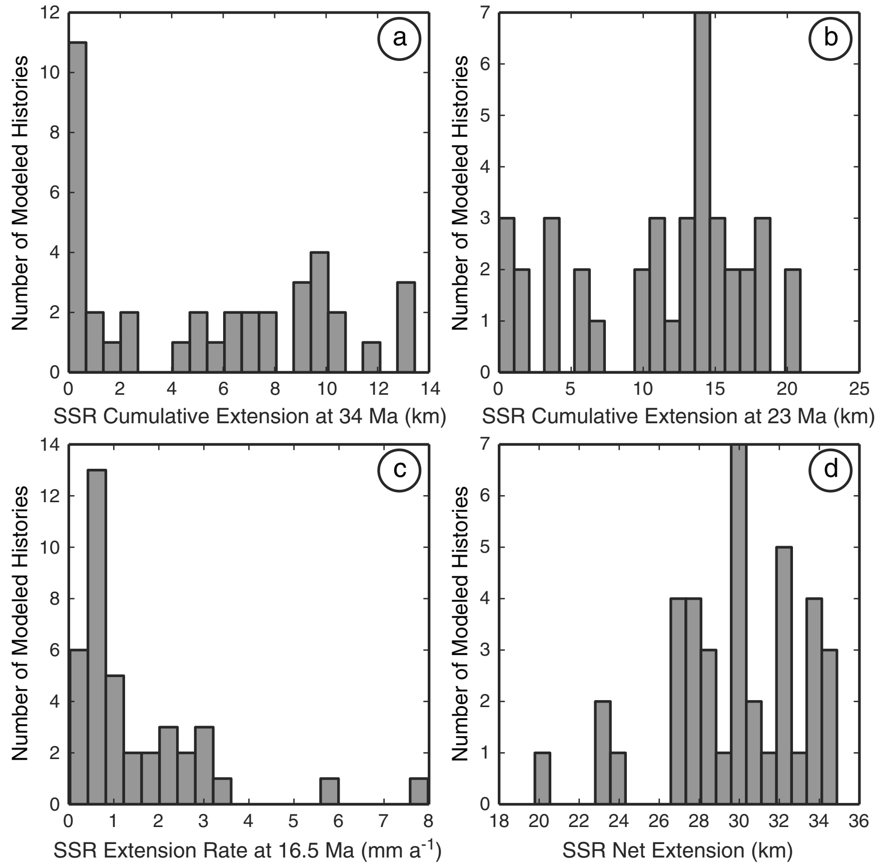

Figure 6. Histograms for the posterior model results of the SSR shown in Figure 5. (a) Cumulative extension at 35 Ma shows a slightly bimodal distribution. Sixteen modeled histories have < 3 km of extension accumulated by 35 Ma. The remaining 23 of 39 modeled histories have > 4 km of extension by 35 Ma. (b) The histogram for cumulative extension at 23 Ma shows 28 of 39 modeled histories have ≥ 10 km of extension accumulated in the SSR. (c) The extension rate at 16.5 Ma is the highest modeled for the SSR. The histogram shows that half of the modeled histories require < 1 mm a^{-1} extension rates, and almost all modeled histories require < 4 mm a^{-1} rates of extension. (d) The majority of the modeled histories (35 of 39) require > 26 km of total net extension in the SSR during the Cenozoic. This extension is accommodated on both the WPF and SSRD structures; however, the earliest onset of extension on the WPF is early Miocene and only accounts for a mean 2.75 km of extension based on the modeled histories.

Figure 5a, the extension rate history for the SSR, shows that throughout the Miocene, when the majority of extension occurred, there is an order-of-magnitude variation in posterior slip rates. However, Figure 5b shows that during the same time, the cumulative exhumation is much more tightly bracketed. The magnitude of cumulative exhumation, combined with the geothermal gradient, directly controls whether a given thermochronometric sample has passed through its thermal sensitivity window (partial retention or partial annealing zone). As a result, the timing of cumulative exhumation is more important for determining cooling ages than the rate at which the samples cool through this window. Additionally, the individual slip rates are generally more ephemeral and noisy than the cumulative extensions. Similarly, Figure 7 shows that the posteriors display more structure (e.g., linear relationships and clustering) when metavariables are plotted (Figures 7d–7f) rather than the Pecube input variables (Figures 7a–7c).

5.6.1. Relationship Between Crustal Heat and Deformation

The model results are not sensitive to particular values for the Moho temperature or radiogenic heat production. However, the results are sensitive to the geothermal gradient, which is a function of both of these variables. More specifically, a trade-off exists between the geothermal gradient and the minimum amount of extension on the SSRD necessary to exhume all thermochronometers from below their partial retention or annealing zones. This is illustrated in Figure 7c: below the dashed line, no posteriors are present; however, above the dashed line, the posteriors are somewhat evenly distributed, indicating this threshold. Because the posteriors

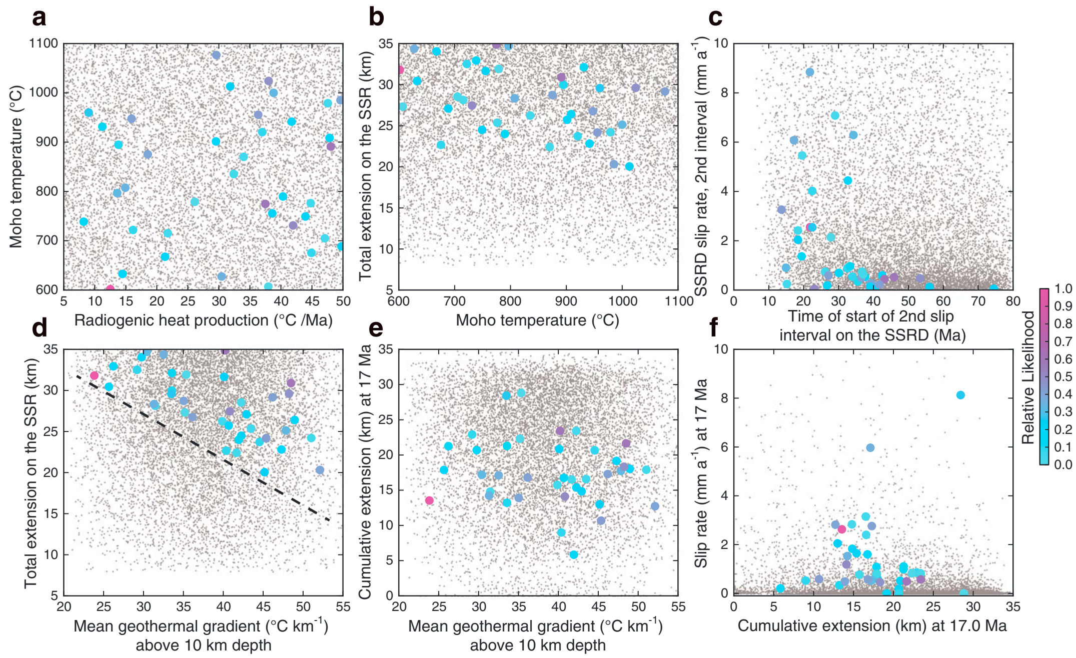

Figure 7. Scatterplots of priors (grey dots) and posteriors (colored circles) for various combinations of variables. Figures 7a–7c show variables directly used in the inversion, whereas Figures 7d–7f show metavariables derived from the input variables which offer more insight into the results, as shown by the distributions of the posteriors. (a) Variables determining the thermal state of the crust; no relationship is observed. (b) Total (i.e., modern) extension across the SSR compared with Moho temperature; no relationship is observed. (c) Timing of the start of the second slip interval on the SSRD versus the slip rate for that interval. Times older than ~30 Ma have very low slip rates, suggesting that little cumulative exhumation occurred during this time; however, if the second interval is younger, faster rates are acceptable. (d) Total SSR extension versus the mean geothermal gradient in the upper crust. The dashed black line indicates a threshold amount of extension required to exhume the thermochonologic samples through their thermal sensitivity windows, which is dependent on the geothermal gradient. (e) Upper crustal geothermal gradients versus cumulative extension at 17 Ma. The posteriors are somewhat more clustered between ~13 and 23 km, relative to the total extension shown in Figure 7b. (f) Cumulative extension versus slip rate at 17 Ma. This plot shows the posteriors to be much more tightly clustered than in Figure 7c.

plot above a line, rather than on a line, we interpret this to be a threshold effect rather than an optimal combination of variables.

6. Discussion

The new (U-Th)/He thermochronologic results combined with fission track data from *Miller et al.* [1999] and Pecube modeling suggest that three significant periods of extension occurred during the Neogene and Paleogene for the SSRD and WPF (Figure 8): (1) ~50–45 to ~38 Ma (Eocene), (2) ~33–30 to ~23 Ma (Oligocene), and (3) ~23–20 to ~10–8 Ma (Miocene). These periods of extension were defined based on clusters of increased extension rates of individual modeling histories (see Figure 5) and does not imply that extension occurred continuously in the SSR during each of the periods. These periods of extension are considered largely driven by tectonic rather than erosional processes based on the denudation rates discussed in section 4.2.

The first two periods of extension most likely occurred on the SSRD and related upper plate structures, while the third period of extension was probably accommodated on both the SSRD and WPF. A younger period of extension during the Miocene, possibly starting at ~10–8 Ma, continuing to present day occurs solely on the WPF (Figure 5), an active range bounding normal fault [*Sawyer*, 1998; *U.S. Geological Survey and Nevada Bureau of Mines and Geology*, 2006]. However, the contribution of this period to the overall extensional history of the SSR is minor.

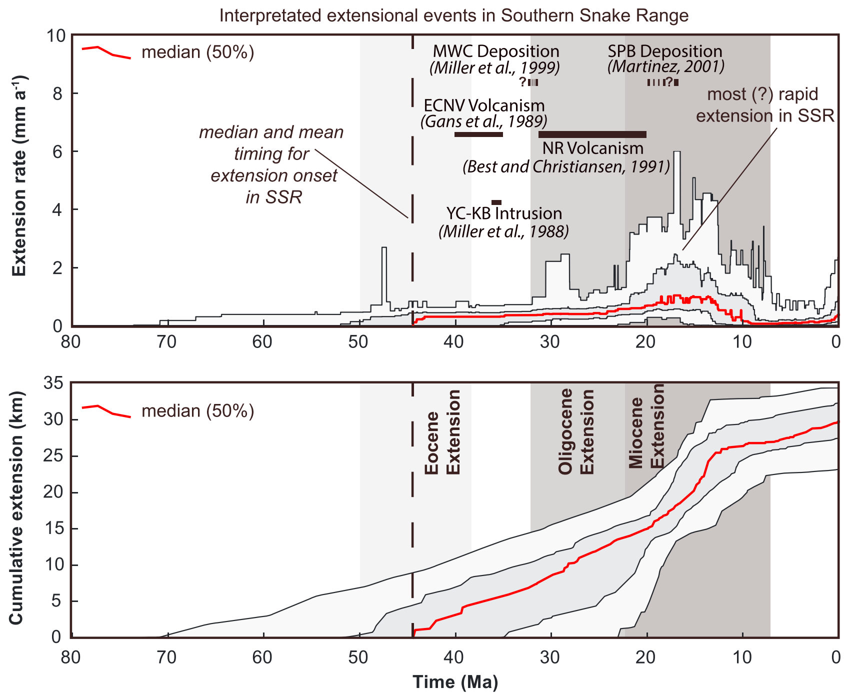

Figure 8. An interpreted plot of the percentile envelopes for the posterior model histories for the SSR from Figure 5. Gray bars show extensional periods discussed in section 6.1. The vertical black dashed line indicates the median and mean onset of extension in the SSR. Thin black line indicates the most rapid period of extension in the SSR from the modeled histories at ~16.5 Ma. The horizontal dashed black lines indicate the relative timing between the deposition of the Murphy Wash conglomerate (MWC) [*Miller et al.*, 1999] in the SSR, development of the Sacramento Pass basin (SPB) [*Martinez*, 2001], and the three periods of extension interpreted from the modeling. Solid black bars denote the timing of magmatism in the immediate region of east-central Nevada [*Miller et al.*, 1988; *Gans et al.*, 1989; *Best and Christiansen*, 1991] relative to defined extensional periods. Abbreviations: MWC = Murphy Wash conglomerate, SPB = Sacramento Pass basin, SSR = Southern Snake Range, ECNV = east-central Nevada, NR = Needles Range, YC-KB = Young Canyon-Kious Basin pluton.

Our modeling results suggest that extension in the SSR could be accommodated, at least in part, on a structure with a dip similar to the SSRD of *McGrew* [1993]. Extension in the SSR has previously been interpreted to occur on a high-angle normal fault during the Miocene that subsequently rotated to the present-day low-angle orientation of the SSRD [*Miller et al.*, 1999]. Our modeling results suggest that tectonic denudation by a low-angle detachment, as shown in the *McGrew* [1993] cross section, also matches the observed distribution of cooling ages. However, our methodology does not preclude the interpretation of *Miller et al.* [1999] because it does not explicitly address the possibility of variable fault geometries (e.g., rotation of fault planes) through time.

Modeled extension in the SSR appears to have been relatively slow throughout much of its history. Despite relatively slow rates, mostly $< 1\ \mathrm{mm\ a^{-1}}$, extension produced a mean cumulative net extension of 29.7 km. Our modeled magnitude of extension in the SSR is higher than the ~15 km of *Miller et al.* [1999] (only estimated for the Miocene) and similar to the upper end of the 8–24 km range for the Cenozoic from *McGrew* [1993]. The discrepancy between our estimate of total net extension and *Miller et al.* [1999] is likely due to significant pre-Miocene extension in the range. Our cumulative net extension estimate for the WPF, 2.8 km, is in good agreement with first-order extension estimates based on an assumed planar high-angle normal fault and depth to basement in Spring Valley from gravity data [*Maniken et al.*, 2007].

6.1. Extension in the SSR and NSR

An Eocene period of extension is documented in the NSR by *Lee* [1995] from ~48 to 41 Ma, similar to the first period of SSR extension. The similarities in timing of extension in the SSR and NSR suggest that the NSRD and SSRD have been intimately linked structures since the Eocene, rather than strictly during rapid extension in the Miocene [e.g., *Miller et al.*, 1999]. *Lee* [1995] only reported cooling rates in the NSR, and as a result, it is impossible to compare rates of extension between the NSRD and SSRD. However, the NSR was significantly more deformed during Cenozoic extension than the SSR [e.g., *Miller et al.*, 1983; *Bartley and Wernicke*, 1984], and it is reasonable to assume that extension rates were faster in the NSR than those suggested by the Pecube modeling for the SSR.

Based on our modeling, the quiescent period between the first and second period of extension in the Oligocene is coincident with plutonism in the SSR at ~36 Ma [*Miller et al*., 1988] and volcanic activity in the region [*Gans et al*., 1989] (Figure 8). It also coincides with a period of slow cooling documented in the NSR [*Lee*, 1995].

Modeled rates of extension increased again in the SSR during the Oligocene at ~33–30 Ma and continued until the Miocene (Figure 8). This second period of extension has not been previously reported for the SSR and occurs during major Needles Range Group volcanism associated with eruptions of the Indian Peak Caldera Complex [e.g., *Best and Grant*, 1987; *Best et al*., 1989; *Best and Christiansen*, 1991]. A similar pulse of Oligocene extension was documented by potassium feldspar MDD modeling [*Lee*, 1995] and by $^{40}Ar/^{39}Ar$ and stable isotope analyses of white mica [*Gébelin et al*., 2011] in the NSR. The similar timing of extension in the NSR and SSR during the Oligocene further substantiates a link between the NSRD and SSRD throughout the Cenozoic.

Our model results show that the most rapid extension in the SSR began during the third extensional period at ~16.5 Ma (Figure 8). Rapid extension was previously interpreted by *Miller et al*. [1999] for the greater Snake Range-Deep Creek fault system at ~17 Ma based on ZrnFT and ApFT data. However, our results show that in the SSR there was an increase in extension rates that started during the early Miocene (~23–20 Ma) and extension rates remained relatively high until the middle Miocene (~10–8 Ma). We interpret this to mean that extension in the SSR occurred over a significantly longer period of time than the short period interpreted by *Miller et al*. [1999].

The mean cumulative net extension for the SSR, 29.7 km, is significantly less than the estimated 60 km of net slip on the Snake Range décollement (NSRD) by *Bartley and Wernicke* [1984]. However, the estimate of slip for the NSRD by *Miller et al*. [1999] is 12–15 km during the Miocene. Our net cumulative extension for the SSR during the Miocene is 15–20 km, only slightly more than estimated for the NSRD by *Miller et al*. [1999].

6.2. Sedimentary Evidence For SSR Extension

Strata preserved within the upper plate of the SSRD corroborate the Eocene and Miocene periods of extension in the SSR suggested by our thermochronologic and modeling results (Figure 8). In the southernmost SSR, a ~40 m thick clast-supported conglomerate containing plutonic and carbonate clasts, informally named the Murphy Wash conglomerate, is capped by the ~31 Ma Cottonwood Wash Tuff (unpublished $^{40}Ar/^{39}Ar$ age reported by *Miller et al*. [1999]). This conglomerate has been used as evidence for pre-31 Ma extension within the SSR, but the timing was only loosely bracketed as latest Eocene to early Oligocene [*Miller et al*., 1999]. Our modeling data suggest that this period of extension occurred from ~50–45 to 38 Ma, and the extension must have created sufficient topography to act as source for this conglomerate. Furthermore, the plutonic clasts, if they are locally derived from the SSR, requires that extension during the Eocene was of sufficient magnitude to expose one or more of the plutonic bodies presently located in the lower plate of the SSRD at the surface. It seems reasonable that these plutonic clasts were locally derived as they are in an areally restricted, thin deposit, and clasts are subrounded to subangular. This relationship between conglomerate deposition and extension in the Eocene suggests that higher estimates for net cumulative extension may be more reasonable than the modeled lower magnitudes prior to 34 Ma (see higher magnitude population in Figure 6a).

During the Oligocene to early Miocene, the Sacramento Pass basin formed between the SSR and NSR [e.g., *Miller et al*., 1999]. The increase in extension rates at ~23 to 20 Ma in the SSR is concurrent with interpreted rock avalanche deposits in the basal Sacramento Pass basin stratigraphy [*Martinez*, 2001], suggesting that the acceleration in extension rates at ~20 Ma in many of the model results is geologically significant.

6.3. Cenozoic Magmatism and Extension in the SSR

Volcanism in east-central Nevada during the Eocene produced andesitic and rhyolitic lava flows (Figure 8) [e.g., *Gans et al*., 1989]. During the Oligocene to early Miocene voluminous ash flow tuffs erupted from the Indian Peak Caldera complex (Figure 8) [e.g., *Best and Grant*, 1987; *Best et al*., 1989; *Best and Christiansen*, 1991; *Best et al*., 2013]. Studies of east-central Nevada volcanism have suggested a spatial and temporal link between the timing of extension and magmatism in the region. *Gans et al*. [1989] interpreted magmatism to have thermally weakened the crust driving the onset of extension, and as a result, the onset of extension in the region was either synmagmatic or immediately post-magmatic. They documented upper crustal extension in east-central Nevada post-eruption of andesite and rhyolite lavas and ash flow tuffs, which initiated at ~40 Ma, and argued that extension was concurrent with the eruption of the Kalamazoo Tuff at ~35 Ma [*Gans et al*., 1989]. *Axen et al*. [1993] interpreted the onset of extension in the northern portion of their "eastern-belt of extension" (includes the SSR) to be either synvolcanism or post-volcanism. In contrast, *Best and Christiansen* [1991] and *Best et al*. [2013] found no evidence for significant, regional-scale synmagmatic extension during Oligocene and early Miocene Needles Range Group volcanism (~31–20 Ma). Our results and interpretations for the timing of extension show no clear relationship between extension and magmatism in the SSR (Figure 8). Extension in the SSR initiates in the Eocene at ~50–45 Ma, based on the modeling results, prior to the east-central Nevada volcanism and extension documented by *Gans et al*. [1989]. Our model interpretations suggest that it is either minor or nonexistent during the intrusion of the Young Canyon-Kious Basin pluton at ~36 Ma [*Miller et al*., 1988] and is significant during and following the eruption of the Needles Range Group [*Best and Grant*, 1987; *Best et al*., 1989; *Best and Christiansen*, 1991]. If strictly interpreted, none of the temporal relationships expected in this region between extension and magmatism [e.g., *Gans et al*., 1989; *Best and Christiansen*, 1991; *Axen et al*., 1993; *Best et al*., 2013] are supported by our new data at the scale of the SSR. This absence of a relationship between extension and magmatism at the scale of a single range is not a new interpretation in the NBR; *Taylor* [1990] documented a similar lack of relationship between volcanism and extension at the scale of the North Pahroc and Seaman Ranges. Further, *Axen et al*. [1993] suggested that local relationships between extension and volcanism may be variable, with extension initiating prior to volcanism and continuing after volcanism, similar to our interpretations from the SSR. It is possible that the SSR is too small scale to record any regionally applicable temporal relationship between extension and magmatism. Larger-scale relationships between extension and magmatism are not refuted by our data [e.g., *Axen et al*., 1993].

6.4. Conceptual Evolution of the SSR

Our new thermochronologic data and Pecube modeling of these data, combined with previously published low-temperature thermochronologic data from *Miller et al*. [1999], allowed us to define three periods of extension in the SSR. A conceptual model for the evolution of the SSR based on these interpretations and ideas from *Armstrong* [1972], *Miller et al*. [1983, 1988], *McGrew* [1993], *Miller et al*. [1999], *Martinez* [2001], and *Long* [2012] is presented in Figure 9. This evolutionary model suggests that extension began earlier, in the Eocene, than previously interpreted from low-temperature thermochronology or conglomerate deposits in the SSR [*Miller et al*., 1999]. Although our data do not preclude even earlier, synconvergence extension, the thermochronologic data and modeling provide no direct evidence for pre-Cenozoic extension in contrast to other portions of the NBR [e.g., *Wells et al*., 1990; *Hodges and Walker*, 1992; *Druschke et al*., 2009; *Long et al*., 2015]. However, our model does incorporate surface breaking extension along the SSRD during the Eocene-Oligocene, based on the cooling of rocks, now exposed at the surface, below ~200–140°C (ZrnPRZ) during the Eocene. Further, we infer that extension on the SSRD was of sufficient magnitude to exhume a footwall pluton to the surface prior to ~31 Ma (Figure 9) based on the presence of plutonic clasts within the Murphy Wash conglomerate. Our modeling corroborates interpretations that extension was more rapid during the Miocene [e.g., *Miller et al*., 1999], but extension most likely occurred over a significantly longer period of time. Finally, extension on both the WPF and SSRD is responsible for creating the geologic relationships observed in the SSR today (Figure 9).

6.5. Regional Context of SSR Extension

Extension in the SSR interpreted from the Pecube modeling is broadly coincident with cooling related to extension in the NSR during the Cenozoic [e.g., *Lee*, 1995]. Extension during the latest Eocene to early Oligocene documented by *Gans et al*. [1989] in east-central Nevada (north of the SSR) overlaps the second period of Oligocene extension in the SSR. Our results and interpretations support coincident extension in the SSR, NSR, Deep Creek Range, and Kern Mountains during the Miocene in agreement with *Miller et al*. [1999]. Previous workers also suggested that the Snake Range décollement (NSRD and SSRD) has a structural link to the Stampede detachment/Seaman breakaway or these structures form a regional extensional belt [e.g., *Taylor*, 1990; *Taylor and Bartley*, 1992; *Axen et al*., 1993]. The timing of extension in the SSR during the Oligocene and Miocene is similar to the periods of extension interpreted by *Taylor* [1990] for the Seaman breakaway; therefore, our new data and models further corroborate a possible structural link between these

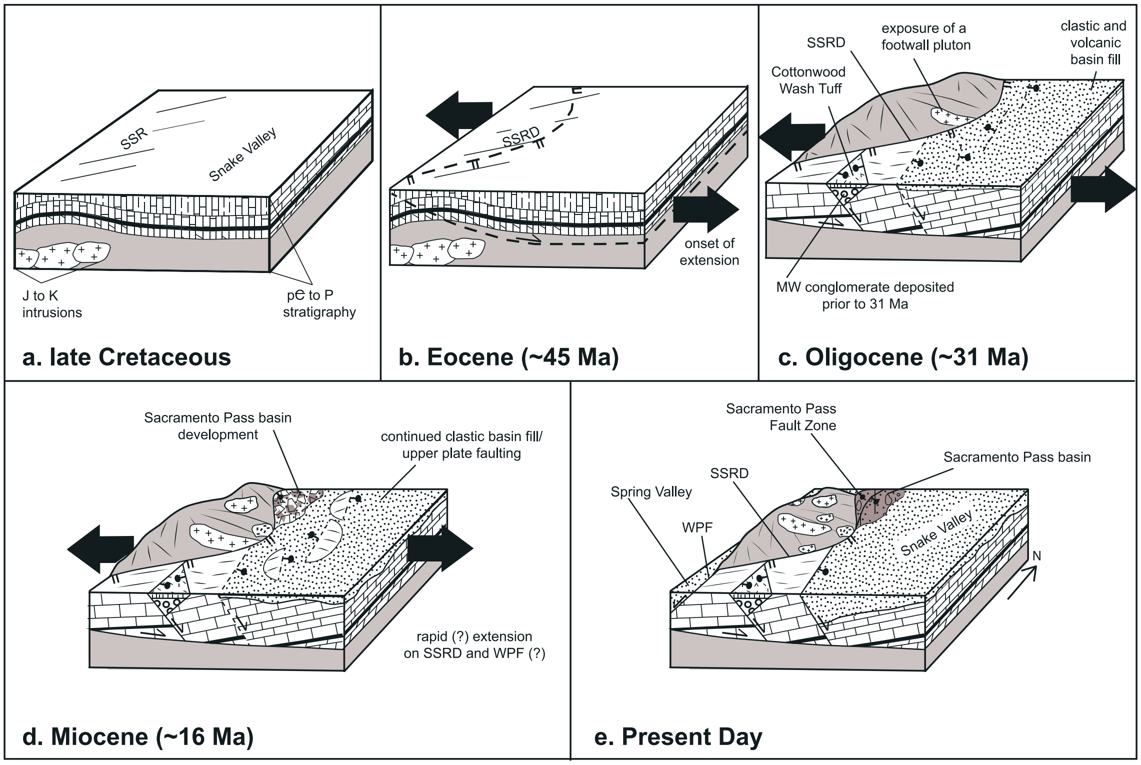

Figure 9. Conceptual evolution of the SSR based on our modeled history of extension in the SSR, and ideas presented in *Armstrong* [1972], *Miller et al*. [1983], *Miller et al*. [1988], *McGrew* [1993], *Miller et al*. [1999], *Martinez* [2001], and *Long* [2012]. These figures are not to scale, and orientations, locations, and stratigraphic offsets are conceptual. (a) Prior to extension during the Cenozoic, the area of the present-day SSR was intruded by Mesozoic plutons, underwent Mesozoic metamorphism, and was broadly folded during the Sevier orogeny [e.g., *Miller et al*., 1988]. No significant structural relief existed in the region based on the relatively flat sub-Tertiary unconformity [e.g., *Armstrong*, 1972; *Miller et al*., 1983; *Long*, 2012]. (b) Based on the posterior model histories the onset of SSR extension occurred at ~45 Ma and was, at least initially, accommodated solely on a structure similar in orientation to the SSRD of *McGrew* [1993]. (c) Extension in the Oligocene began at ~33 Ma following a period of relative quiescence in the late Eocene based on our model histories. Exposure of a footwall pluton at the surface prior to or during the early Oligocene is necessary if the plutonic clasts present in the Murphy Wash conglomerate beneath the Cottonwood Wash Tuff [*Miller et al*., 1999] are locally derived. (d) Rapid Miocene extension occurred and was concurrent with the development of the Sacramento Pass basin [*Martinez*, 2001]. (e) A present-day conceptual block diagram for the SSR based on *Miller et al*. [1999] and *McGrew* [1993]. Abbreviations: SSR = Southern Snake Range, J = Jurassic, K = Cretaceous, pC = pre-Cambrian, P = Permian, SSRD = Southern Snake Range Décollement, MW = Murphy Wash, WPF = Wheeler Peak Fault.

detachment systems during at least the Oligocene and Miocene. The interpreted periods of extension in the SSR, from our modeling of low-temperature thermochronometers, are also broadly coincident with extension during the Cenozoic in the Raft River-Albion-Grouse Creek MCC and Ruby-East Humboldt MCC [e.g., *Dallmeyer et al*., 1986; *Saltzer and Hodges*, 1988; *Mueller and Snoke*, 1993; *McGrew and Snee*, 1994; *Wells et al*., 2000; *Colgan and Henry*, 2009; *Colgan et al*., 2010; *Konstantinou et al*., 2012].

Our new data and model interpretations suggest an onset of extension and possible collapse of the Nevadaplano prior to ~17 Ma [e.g., *Colgan and Henry*, 2009]. The new data and model interpretations do not constrain whether the upper crustal extension in the SSR during the Eocene and Oligocene represents extension that directly contributed to the collapse of the Nevadaplano. However, the magnitude of extension by the Oligocene-Miocene boundary in the SSR is between ~10 and 18 km for most model histories (Figure 6b), suggesting that a significant amount of extension occurred in this area prior to ~17 Ma. It is possible that the extension in the SSR represents early onset extensional collapse of the eastern Nevadaplano prior to collapse in the western portion of the plateau at ~17 Ma [e.g., *Colgan and Henry*, 2009].

7. Conclusions

The integration of low-temperature thermochronology and Bayesian thermokinematic modeling suggests that extension in the SSR was episodic throughout the Cenozoic. These results allowed us to address the five questions initially proposed in this study as follows:

1. The new thermochronologic data and interpreted modeling results suggest that around half of the extension within the SSR occurred pre-Miocene. Eocene and Oligocene extensional magnitudes are significant compared to overall extension in the SSR, and cooling during this time is well documented by the thermochronologic data. This contrasts with *Miller et al*. [1999] who interpreted the majority of extension to be Miocene in age. The rate of extension was relatively low throughout the Cenozoic in the SSR at $< 0.5\,\mathrm{mm\,a^{-1}}$; however, individual modeling histories suggest periods of rapid extension rates, especially at ~16.5 Ma. These modeling histories are in agreement with the period of rapid extension reported by *Miller et al*. [1999] during the Miocene.
2. Three significant periods of extension in the SSR were defined based on modeling results at ~50–45 to ~38 Ma (Eocene), ~33–30 to ~23 Ma (Oligocene), and ~23–20 to ~10–8 Ma (Miocene). These three periods of modeled extension in the SSR are broadly coincident with cooling related to extension in the NSR [e.g., *Lee*, 1995].
3. The magnitude of extension in the SSR based on modeling ranges from 19.8 to 34.9 km for all modeled histories and has a mean value of 29.7 km. This total magnitude is slightly higher than the estimate by *McGrew* [1993] based on a palinspastic reconstruction of the SSR. Our estimate for the total magnitude of extension in the SSR is also higher than estimates for the SSRD reported by *Miller et al*. [1999]; however, their estimate only included extension on the SSRD during the Miocene, whereas our estimate is for the entire Cenozoic.
4. The new and previously published low-temperature thermochronologic data for the SSR are exclusively Cenozoic and thus do not speak to the issue of whether or not there was significant Cretaceous extension in this range as has been suggested for other parts of the NBR. The models were built to permit the possibility of an initiation of extensional activity in the Cretaceous, but the modeling results showed that such an early start is not required by the available low-temperature thermochronologic data.
5. Overall, the timing of Cenozoic extension in the SSR was similar to Cenozoic extension in the NSR [e.g., *Lee*, 1995; *Miller et al*., 1999] and in other areas of east-central Nevada [e.g., *Gans et al*., 1989; *Taylor*, 1990]. Extension and magmatism in the SSR have no clear temporal relationship; however, regional-scale relationships [e.g., *Gans et al*., 1989; *Best and Christiansen*, 1991; *Axen et al*., 1993; *Best et al*., 2013] are not ruled out. Our interpreted periods of extension in the SSR further support a large-scale extensional belt in east-central Nevada during the Oligocene and Miocene stretching from the Stampede detachment/Seaman breakaway, through the SSR, and north to the NSR, Deep Creek Range, and Kern Mountains [e.g., *Taylor*, 1990; *Taylor and Bartley*, 1992]. Given the timing of extension from the Eocene to Miocene in east-central Nevada and magnitude of extension we documented for the SSR, it is possible that extensional collapse of the Nevadaplano in this region began well before the ~17 Ma time frame suggested for the NBR to the west and north of our study area [e.g., *Colgan and Henry*, 2009].

Acknowledgments

This research was funded in part by grants from the Graduate Professional and Student Association of the University of Nevada, Las Vegas (Evans), the Nevada Petroleum and Geothermal Society (Evans), the Geological Society of America Grant-in-Aid (Evans), Fay and Jack Ross Fellowship of the University of Nevada, Las Vegas (Evans), and Department of the Interior (Hanson). Joseph Miller provided field assistance in the collection of (U-Th)/He thermochronologic samples. Michelle Aigner provided laboratory assistance in the mineral separation of (U-Th)/He samples at Arizona State University. Ron Young provided help with running codes on the Eureka cluster at the National Supercomputing Center for Energy and the Environment of the University of Nevada, Las Vegas. Modeled thermochronologic age data are available in the paper or cited in the paper. Pecube modeling code availability is described by a reference cited in the paper [*Braun et al*., 2012]. All code used in the modeling and generation of Figures 3–7 is publicly archived and available at https://github.com/cossatot/ssrd_pecube. All other data used to create figures are cited and referenced in the paper. Brenda Buck, Terry Spell, Wanda Taylor, and two anonymous reviewers are thanked for comments that improved this manuscript.

References

Allmendinger, R. W., J. W. Sharp, D. Von Tish, L. Serpa, L. Brown, S. Kaufman, J. Oliver, and R. B. Smith (1983), Cenozoic and Mesozoic structure of the eastern Basin and Range province, Utah, from COCORP seismic-reflection data, *Geology*, *11*(9), 532–536, doi:10.1130/0091-7613(1983)11<532:CAMSOT>2.0.CO;2.

Armstrong, R. L. (1972), Low-angle (denudation) faults, hinterland of the Sevier orogenic belt, eastern Nevada and western Utah, *Geol. Soc. Am. Bull.*, *83*(6), 1729–1754, doi:10.1130/0016-7606(1972)83[1729LDFHOT]2.0.CO;2.

Axen, G. J., W. J. Taylor, and J. M. Bartley (1993), Space-time patterns and tectonic controls of Tertiary extension and magmatism in the Great Basin of the western United States, *Geol. Soc. Am. Bull.*, *105*(1), 56–76, doi:10.1130/00167606(1993)105<0056:STPATC>2.3.CO;2.

Bartley, J. M., and B. P. Wernicke (1984), The Snake Range décollement interpreted as a major extensional shear zone, *Tectonics*, *3*(6), 647–657, doi:10.1029/TC003i006p00647.

Best, M. G., and E. H. Christiansen (1991), Limited extension during peak Tertiary volcanism, Great Basin of Nevada and Utah, *J. Geophys. Res.*, *96*(B8), 13,509–13,528, doi:10.1029/91JB00244.

Best, M. G., and S. K. Grant (1987), Stratigraphy of the volcanic Oligocene Needles Range Group in southwestern Utah and eastern Nevada, *U.S. Geol. Surv. Prof. Pap.*, *1433A*, 3–28.

Best, M. G., E. H. Christiansen, A. L. Deino, C. Gromme, E. H. McKee, and D. C. Noble (1989), Eocene through Miocene volcanism in the Great Basin of the western United States, *N. M. Bur. Mines Miner. Resour. Mem.*, *47*, 91–133.

Best, M. G., E. H. Christiansen, and S. Gromme (2013), Introduction: The 36–18 Ma southern Great Basin, USA, ignimbrite province and flareup: Swarms of subduction-related supervolcanoes, *Geosphere*, *9*(2), 260–274, doi:10.1130/GES00870.1.

Braun, J. (2003), Pecube: A new finite-element code to solve the 3D heat transport equation including the effects of a time-varying, finite amplitude surface topography, *Comput. Geosci.*, *29*(6), 787–794, doi:10.1016/S0098-3004(03)00052-9.

Braun, J., P. Van Der Beek, P. Valla, X. Robert, F. Herman, C. Glotzbach, V. Pedersen, C. Perry, T. Simon-Labric, and C. Prigent (2012), Quantifying rates of landscape evolution and tectonic processes by thermochronology and numerical modeling of crustal heat transport using PECUBE, *Tectonophysics*, *524–525*, 1–28, doi:10.1016/j.tecto.2011.12.035.

Buck, W. R. (1991), Modes of continental lithospheric extension, *J. Geophys. Res.*, *96*(B12), 20,161–20,178, doi:10.1029/91JB01485.

Colgan, J. P., and C. D. Henry (2009), Rapid middle Miocene collapse of the Mesozoic orogenic plateau in north-central Nevada, *Int. Geol. Rev.*, *51*(9–11), 920–961, doi:10.1080/00206810903056731.

Colgan, J. P., T. A. Dumitru, P. W. Reiners, J. L. Wooden, and E. L. Miller (2006), Cenozoic tectonic evolution of the Basin and Range Province in northwestern Nevada, *Am. J. Sci.*, *306*(8), 616–654, doi:10.2475/08.2006.02.

Colgan, J. P., K. A. Howard, R. J. Fleck, and J. L. Wooden (2010), Rapid middle Miocene extension and unroofing of the southern Ruby Mountains, Nevada, *Tectonics*, *29*, TC6022, doi:10.1029/2009TC002655.

Coney, P. J., and T. A. Harms (1984), Cordilleran metamorphic core complexes: Cenozoic extensional relics of Mesozoic compression, *Geology*, *12*(9), 550–554, doi:10.1130/0091-7613(1984)12<550:CMCCCE>2.0.CO;2.

Cooper, F., J. Platt, R. Anczkiewicz, and M. Whitehouse (2010), Footwall dip of a core complex detachment fault: Thermobarometric constraints from the northern Snake Range (Basin and Range, USA), *J. Metamorph. Geol.*, *28*(9), 997–1020, doi:10.1111/j.1525-1314.2010.00907.x.

Dallmeyer, R., A. Snoke, and E. McKee (1986), The Mesozoic-Cenozoic tectonothermal evolution of the Ruby Mountains, East Humboldt Range, Nevada: A Cordilleran metamorphic core complex, *Tectonics*, *5*(6), 931–954, doi:10.1029/TC005i006p00931.

DeCelles, P. G. (2004), Late Jurassic to Eocene evolution of the Cordilleran thrust belt and foreland basin system, western USA, *Am. J. Sci.*, *304*(2), 105–168, doi:10.2475/ajs.304.2.105.

DeCelles, P. G., and J. C. Coogan (2006), Regional structure and kinematic history of the Sevier fold-and-thrust belt, central Utah, *Geol. Soc. Am. Bull.*, *118*(7–8), 841–864, doi:10.1130/B25759.1.

DePolo, C. (2008), Quaternary faults of Nevada Nevada Bureau of Mines and Geology Map M167, 1:1,000,000 scale, 1 p.

Dickinson, W. R. (2006), Geotectonic evolution of the Great Basin, *Geosphere*, *2*(7), 353–368, doi:10.1130/GES00054.1.

Dodson, M. (1979), Theory of cooling ages, in *Lectures in Isotope Geology*, edited by E. Jager and J. C. Hunziker, pp. 194–202, Springer, New York.

Dohrenwend, J. C., B. A. Schell, C. M. Menges, B. C. Moring, and M. A. McKittrick (1996), Reconnaissance photogeologic map of young (Quaternary and late Tertiary) faults in Nevada, Nevada Bureau of Mines and Geology Open File Rep., 96–2, 9-1-9-12.

Drewes, H. (1958), Structural geology of the southern Snake Range, Nevada, *Geol. Soc. Am. Bull.*, *69*(2), 221–240, doi:10.1130/0016-7606(1958)69[221:SGOTSS]2.0.CO;2.

Druschke, P., A. D. Hanson, M. L. Wells, T. Rasbury, D. F. Stockli, and G. Gehrels (2009), Synconvergent surface-breaking normal faults of Late Cretaceous age within the Sevier hinterland, east-central Nevada, *Geology*, *37*(5), 447–450, doi:10.1130/G25546A.1.

Ehlers, T. A., and K. A. Farley (2003), Apatite (U–Th)/He thermochronometry: Methods and applications to problems in tectonic and surface processes, *Earth Planet. Sci. Lett.*, *206*(1), 1–14, doi:10.1016/S0012-821X(02)01069-5.

Farley, K. (2000), Helium diffusion from apatite: General behavior as illustrated by Durango fluorapatite, *J. Geophys. Res.*, *105*(B2), 2903–2914, doi:10.1029/1999JB900348.

Farley, K., R. Wolf, and L. Silver (1996), The effects of long alpha-stopping distances on (UTh)/He ages, *Geochim. Cosmochim. Acta*, *60*(21), 4223–4229, doi:10.1016/S0016-7037(96)00193-7.

Farley, K. A. (2002), (U-Th)/He dating: Techniques, calibrations, and applications, *Rev. Mineral. Geochem.*, *47*(1), 819–844, doi:10.2138/rmg.2002.47.18.

Farr, T. G., P. A. Rosen, E. Caro, R. Crippen, R. Duren, S. Hensley, M. Kobrick, M. Paller, E. Rodriguez, and L. Roth (2007), The shuttle radar topography mission, *Rev. Geophys.*, *45*, RG2004, doi:10.1029/2005RG000183.

Flowers, R., B. Wernicke, and K. Farley (2008), Unroofing, incision, and uplift history of the southwestern Colorado Plateau from apatite (U-Th)/He thermochronometry, *Geol. Soc. Am. Bull.*, *120*(5–6), 571–587, doi:10.1130/B26231.1.

Flowers, R. M., R. A. Ketcham, D. L. Shuster, and K. A. Farley (2009), Apatite (U–Th)/He thermochronometry using a radiation damage accumulation and annealing model, *Geochim. Cosmochim. Acta*, *73*(8), 2347–2365, doi:10.1016/j.epsl.2006.07.028.

Foster, D. A., and B. E. John (1999), Quantifying tectonic exhumation in an extensional orogeny with thermochronology: Examples from the southern Basin and Range Province, *Spec. Publ. Geol. Soc. London*, *154*(1), 343–364, doi:10.1144/GSL.SP.1999.154.01.16.

Gans, P., E. Miller, J. McCarthy, and M. Ouldcott (1985), Tertiary extensional faulting and evolving ductile-brittle transition zones in the northern Snake Range and vicinity: New insights from seismic data, *Geology*, *13*(3), 189–193, doi:10.1130/0091-7613(1985)13<189:TEFAED>2.0.CO;2.

Gans, P. B. (1987), An open-system, two-layer crustal stretching model for the Eastern Great Basin, *Tectonics*, *6*(1), 1–12, doi:10.1029/TC006i001p00001.

Gans, P. B., G. A. Mahood, and E. Schermer (1989), Synextensional magmatism in the Basin and Range Province: A case study from the eastern Great Basin, *Geol. Soc. Am. Spec. Pap.*, *233*, 1–53, doi:10.1130/SPE233-p1.

Gébelin, A., A. Mulch, C. Teyssier, M. Heizler, T. Vennemann, and N. C. Seaton (2011), Oligo-Miocene extensional tectonics and fluid flow across the Northern Snake Range detachment system, Nevada, *Tectonics*, *30*, TC5010, doi:10.1029/2010TC002797.

Gorynski, K. E., D. F. Stockli, and J. Douglas Walker (2013), Thermochronometrically constrained anatomy and evolution of a Miocene extensional accommodation zone and tilt domain boundary: The southern Wassuk Range, Nevada, *Tectonics*, *32*, 516–539, doi:10.1002/tect.20044.

Guenthner, W. R., P. W. Reiners, R. A. Ketcham, L. Nasdala, and G. Giester (2013), Helium diffusion in natural zircon: Radiation damage, anisotropy, and the interpretation of zircon (U-Th)/He thermochronology, *Am. J. Sci.*, *313*(3), 145–198, doi:10.2475/03.2013.01.

Hodges, K., and J. Walker (1992), Extension in the Cretaceous Sevier orogen, North American Cordillera, *Geol. Soc. Am. Bull.*, *104*(5), 560–569, doi:10.1130/0016-7606(1992)104<0560:EITCSO>2.3.CO;2.

Hourigan, J. K., P. W. Reiners, and M. T. Brandon (2005), U-Th zonation-dependent alpha ejection in (U-Th)/He chronometry, *Geochim. Cosmochim. Acta*, *69*(13), 3349–3365, doi:10.1016/j.gca.2005.01.024.

House, M. A., B. P. Wernicke, and K. A. Farley (1998), Dating topography of the Sierra Nevada, California, using apatite (U–Th)/He ages, *Nature*, *396*(6706), 66–69, doi:10.1038/23926.

House, M. A., K. A. Farley, and B. P. Kohn (1999), An empirical test of helium diffusion in apatite: Borehole data from the Otway basin, Australia, *Earth Planet. Sci. Lett.*, *170*(4), 463–474, doi:10.1016/S0012-821X(99)00120-X.

John, B. E., and D. A. Foster (1993), Structural and thermal constraints on the initiation angle of detachment faulting in the southern Basin and Range: The Chemehuevi Mountains case study, *Geol. Soc. Am. Bull.*, *105*(8), 1091–1108, doi:10.1130/0016-7606(1993)105<1091:SATCOT>2.3.CO;2.

Ketcham, R. A. (2005), Forward and inverse modeling of low-temperature thermochronometry data, *Rev. Mineral. Geochem.*, *58*(1), 275–314, doi:10.2138/rmg.2005.58.11.

Konstantinou, A., A. Strickland, E. L. Miller, and J. P. Wooden (2012), Multistage Cenozoic extension of the Albion–Raft River–Grouse Creek metamorphic core complex: Geochronologic and stratigraphic constraints, *Geosphere*, *8*(6), 1429–1466, doi:10.1130/GES00778.1.

Kreemer, C., G. Blewitt, and W. C. Hammond (2010), Evidence for an active shear zone in southern Nevada linking the Wasatch fault to the Eastern California shear zone, *Geology*, *38*(5), 475–478, doi:10.1130/G30477.1.

Lee, D., and E. Christiansen (1983), The granite problem as exposed in the southern Snake Range, Nevada, *Contrib. Mineral. Petrol.*, *83*(1–2), 99–116.

Lee, D., R. Marvin, and H. Mehnert (1980), Geologic studies in White Pine County, Nevada: A radiometric age study of Mesozoic-Cenozoic metamorphism in eastern White Pine County, Nevada, and nearby Utah, *U.S. Geol. Surv. Prof. Pap.*, *1158*, 17–28.

Lee, D., J. Stacey, and L. Fischer (1986), Muscovite phenocrystic two mica granites of northeastern Nevada are Late Cretaceous in age, in *Shorter Contributions to Isotope Research*, *U.S. Geol. Surv. Bull*., vol. B1622, edited by Z. E. Peterman and D. C. Schanbel, pp. 31–39, U.S. Gov. Print. Off., Washington, D. C.

Lee, D. E., T. Stern, R. Mays, and R. Van Loenen (1968), Accessory zircon from granitoid rocks of the Mount Wheeler mine area, Nevada, *U.S. Geol. Surv. Prof. Pap.*, *600-D*, D197–D203.

Lee, D. E., R. F. Marvin, T. Stern, and Z. E. Peterman (1970), Modification of potassium-argon ages by Tertiary thrusting in the Snake Range, White Pine County, Nevada, *U.S. Geol. Surv. Prof. Pap.*, *700-D*, D92–D102.

Lee, D. E., R. E. Van Loenen, and R. Mays (1973), Accessory apatite from hybrid granitoid rocks of the southern Snake Range, Nevada, *J. Res. U.S. Geol. Surv.*, *1*, 89–98.

Lee, J. (1995), Rapid uplift and rotation of mylonitic rocks from beneath a detachment fault: Insights from potassium feldspar ^{40}Ar/^{39}Ar thermochronology, northern Snake Range, Nevada, *Tectonics*, *14*(1), 54–77, doi:10.1029/94TC01508.

Lee, J., and J. F. Sutter (1991), Incremental ^{40}Ar/^{39}Ar thermochronology of mylonitic rocks from the northern Snake Range, Nevada, *Tectonics*, *10*(1), 77–100, doi:10.1029/90TC01931.

Lewis, C. J., B. P. Wernicke, J. Selverstone, and J. M. Bartley (1999), Deep burial of the footwall of the northern Snake Range décollement, Nevada, *Geol. Soc. Am. Bull.*, *111*(1), 39–51, doi:10.1130/0016-7606(1999)111<0039:DBOTFO>2.3.CO;2.

Long, S. P. (2012), Magnitudes and spatial patterns of erosional exhumation in the Sevier hinterland, eastern Nevada and western Utah, USA: Insights from a Paleogene paleogeologic map, *Geosphere*, *8*(4), 881–901, doi:10.1130/GES00783.1.

Long, S. P., S. N. Thomson, P. W. Reiners, and R. V. Di Fiori (2015), Synorogenic extension localized by upper-crustal thickening: An example from the Late Cretaceous Nevadaplano, *Geology*, *43*(4), 351–354, doi:10.1130/G36431.1.

MacCready, T., A. W. Snoke, J. E. Wright, and K. A. Howard (1997), Mid-crustal flow during Tertiary extension in the Ruby Mountains core complex, Nevada, *Geol. Soc. Am. Bull.*, *109*(12), 1576–1594, doi:10.1130/0016-7606(1997)109<1576:MCFDTE>2.3.CO;2.

Mankinen, E. A., C. W. Roberts, E. H. McKee, B. A. Chuchel, and R. L. Morin (2007), Geophysical data from Spring Valley to Delamar Valley, east-central Nevada, U.S. Geol. Surv. Open File Rep. 2007–1190, pp. 42.

Martinez, C. M. (2001), Characteristics of sedimentary basins formed above low-angle detachment faults: Examples from the Basin and Range province, western US, paper 1610 presented at Geological Society of America Abstracts with Program, Annual meeting, 5–8 Nov.

McGrew, A. J. (1993), The origin and evolution of the southern Snake Range décollement, east central Nevada, *Tectonics*, *12*(1), 21–34, doi:10.1029/92TC01713.

McGrew, A. J., and E. L. Miller (1995), Geologic map of Kious Spring and Garrison 7.5′ quadrangles, White Pine County, Nevaa and Millard County, Utah, U.S. Geol. Surv. Open File Rep. OF-95-10, scale 1:24,000, 20 p.

McGrew, A. J., and L. W. Snee (1994), ^{40}Ar/^{39}Ar thermochronologic constraints on the tectonothermal evolution of the Northern East Humboldt range metamorphic core complex, Nevada, *Tectonophysics*, *238*(1), 425–450, doi:10.1016/0040-1951(94)90067-1.

Miller, E. L., and P. B. Gans (1989), Cretaceous crustal structure and metamorphism in the hinterland of the Sevier thrust belt, western US Cordillera, *Geology*, *17*(1), 59–62, doi:10.1130/0091-7613(1989)017<0059:CCSAMI>2.3.CO;2.

Miller, E. L., P. B. Gans, and J. Garing (1983), The Snake Range décollement: An exhumed mid-Tertiary ductile-brittle transition, *Tectonics*, *2*(3), 239–263, doi:10.1029/TC002i003p00239.

Miller, E. L., P. B. Gans, J. E. Wright, and J. F. Sutter (1988), Metamorphic history of the east-central Basin and Range province: Tectonic setting and relationship to magmatism, in *Metamorphism and Crustal Evolution, Western Counterminous United States*, edited by W. G. Ernst, pp. 649–682, Prentice-Hall, Englewood Cliffs, N. J.

Miller, E. L., M. M. Miller, C. H. Stevens, J. E. Wright, and R. Madrid (1992), Late Paleozoic paleogeographic and tectonic evolution of the western US Cordillera, in *The Cordilleran Orogen: Conterminous U.S*, vol. G-3, edited by B. C. Burchfiel, P. W. Lipman, and M. L. Zoback, pp. 57–106, Geol. Soc. of Am., Boulder, Colo.

Miller, E. L., T. A. Dumitru, R. W. Brown, and P. B. Gans (1999), Rapid Miocene slip on the Snake Range–Deep Creek Range fault system, east-central Nevada, *Geol. Soc. Am. Bull.*, *111*(6), 886–905, doi:10.1130/0016-7606(1999)111<0886:RMSOTS>2.3.CO;2.

Misch, P. (1960), Regional structural reconnaissance in central-northeast Nevada and some adjacent areas: Observations and interpretations, Intermountain Association of Petroleum Geologists Guidebook for 11th Annual Field Conference, 17–42.

Mosegaard, K., and A. Tarantola (1995), Monte Carlo sampling of solutions to inverse problems, *J. Geophys. Res.*, *100*(B7), 12,431–12,447, doi:10.1029/94JB03097.

Mueller, K. J., and A. W. Snoke (1993), Progressive overprinting of normal fault systems and their role in Tertiary exhumation of the East Humboldt-Wood Hills Metamorphic Complex northeast Nevada, *Tectonics*, *12*(2), 361–371, doi:10.1029/92TC01967.

Pearson, R. K. (2011), *Exploring Data in Engineering, the Sciences, and Medicine*, 792 pp., Oxford Univ. Press, New York.

Poole, F. G., J. H. Stewart, A. R. Palmer, C. A. Sandberg, R. J. Madrid, R. J. Ross, L. F. Hintze, M. M. Miller, and C. T. Wrucke (1992), Latest Precambrian to Devonian time: Development of a continental margin, in *The Cordilleran Orogen: Conterminous U.S*, vol. G-3, edited by B. C. Burchfiel, P. W. Lipman, and M. L. Zoback, pp. 9–56, Geol. Soc. of Am., Boulder, Colo.

Portenga, E. W., and P. R. Bierman (2011), Understanding Earth's eroding surface with ^{10}Be, *GSA Today*, *21*(8), 4–10, doi:10.1130/G111A.1.

Reiners, P. W. (2005), Zircon (U-Th)/He thermochronometry, *Rev. Mineral. Geochem.*, *58*(1936), 151–179, doi:10.2138/rmg.2005.58.6.

Reiners, P. W., and M. T. Brandon (2006), Using thermochronology to understand orogenic erosion, *Annu. Rev. Earth Planet. Sci.*, *34*, 419–466, doi:10.1146/annurev.earth.34.031405.125202.

Saltzer, S., and K. Hodges (1988), The Middle Mountain shear zone, southern Idaho: Kinematic analysis of an early Tertiary high-temperature detachment, *Geol. Soc. Am. Bull.*, *100*(1), 96–103.

Sambridge, M. (1999), Geophysical inversion with a neighbourhood algorithm—I. Searching a parameter space, *Geophys. J. Int.*, *138*(2), 479–494, doi:10.1046/j.1365-246X.1999.00876.x.

Sambridge, M., and K. Mosegaard (2002), Monte Carlo methods in geophysical inverse problems, *Rev. Geophys.*, *40*(3), 1009, doi:10.1029/2000RG000089.

Sawyer, T. L. (Comp) (1998), Fault number 1430, Wheeler Peak fault zone, in *Quaternary Fault and Fold Database of the United States*, *U.S. Geol. Surv*. [Available at http://earthquakes.usgs.gov/hazards/qfaults, accessed 15 Feb. 2014]

Schildgen, T. F., T. A. Ehlers, D. M. Whipp, M. C. van Soest, K. X. Whipple, and K. V. Hodges (2009a), Quantifying canyon incision and Andean Plateau surface uplift, southwest Peru: A thermochronometer and numerical modeling approach, *J. Geophys. Res.*, *114*, F04014, doi:10.1029/2009JF001305.

Schildgen, T. F., K. V. Hodges, K. X. Whipple, M. S. Pringle, M. van Soest, and K. Cornell (2009b), Late Cenozoic structural and tectonic development of the western margin of the Central Andean Plateau in southwest Peru, *Tectonics*, *28*, TC4007, doi:10.1029/2008TC002403.

Shuster, D. L., R. M. Flowers, and K. A. Farley (2006), The influence of natural radiation damage on helium diffusion kinetics in apatite, *Earth Planet. Sci. Lett.*, *249*(3), 148–161, doi:10.1016/j.epsl.2006.07.028.

Snell, K. E., P. L. Koch, P. Druschke, B. Z. Foreman, and J. M. Eiler (2014), High elevation of the 'Nevadaplano' during the Late Cretaceous, *Earth Planet. Sci. Lett.*, *386*, 52–63, doi:10.1016/j.epsl.2013.10.046.

Sonder, L. J., and C. H. Jones (1999), Western United States extension: How the west was widened, *Annu. Rev. Earth Planet. Sci.*, *27*(1), 417–462, doi:10.1146/annurev.earth.27.1.417.

Stockli, D. F. (2005), Application of low-temperature thermochronometry to extensional tectonic settings, *Rev. Mineral. Geochem.*, *58*(1936), 411–448, doi:10.2138/rmg.2005.58.16.

Stockli, D. F., K. A. Farley, and T. A. Dumitru (2000), Calibration of the apatite (U-Th)/He thermochronometer on an exhumed fault block, White Mountains, California, *Geology*, *28*(11), 983–986, doi:10.1130/0091-7613(2000)28<983:COTAHT>2.0.CO;2.

Stockli, D. F., B. E. Surpless, T. A. Dumitru, and K. A. Farley (2002), Thermochronological constraints on the timing and magnitude of Miocene and Pliocene extension in the central Wassuk Range, western Nevada, *Tectonics*, *21*(4), 1028, doi:10.1029/2001TC001295.

Stockli, D. F., T. A. Dumitru, M. O. McWilliams, and K. A. Farley (2003), Cenozoic tectonic evolution of the White Mountains, California and Nevada, *Geol. Soc. Am. Bull.*, *115*(7), 788–816, doi:10.1130/0016-7606(2003)115<0788:CTEOTW>2.0.CO;2.

Styron, R. H., M. H. Taylor, K. E. Sundell, D. F. Stockli, J. A. Oalmann, A. Möller, A. T. McCallister, D. Liu, and L. Ding (2013), Miocene initiation and acceleration of extension in the South Lunggar rift, western Tibet: Evolution of an active detachment system from structural mapping and (U-Th)/He thermochronology, *Tectonics*, *32*(4), 880–907, doi:10.1002/tect.20053.

Tarantola, A. (2005), *Inverse Problem Theory: Methods for Data Fitting and Model Parameter Estimation*, 630 pp., Elsevier, Amsterdam, Netherlands.

Taylor, W. J. (1990), Spatial and temporal relations of Cenozoic volcanism and extension in the North Pahroc and Seaman Ranges, eastern Nevada, *Geol. Soc. Am. Mem.*, *176*, 181–194, doi:10.1130/MEM176-p181.

Taylor, W. J., and J. M. Bartley (1992), Prevolcanic extensional Seaman breakaway fault and its geologic implications for eastern Nevada and western Utah, *Geol. Soc. Am. Bull.*, *104*(3), 255–266, doi:10.1130/0016-7606(1992)104<0255:PESBFA>2.3.CO;2.

Taylor, W. J., J. M. Bartley, M. W. Martin, J. W. Geissman, J. D. Walker, P. A. Armstrong, and J. E. Fryxell (2000), Relations between hinterland and foreland shortening: Sevierorogeny, central North American Cordillera, *Tectonics*, *19*(6), 1124–1143, doi:10.1029/1999TC001141.

Trexler, J. H., P. H. Cashman, W. S. Snyder, and V. I. Davydov (2004), Late Paleozoic tectonism in Nevada: Timing, kinematics, and tectonic significance, *Geol. Soc. Am. Bull.*, *116*(5–6), 525–538, doi:10.1130/B25295.1.

U.S. Geological Survey and Nevada Bureau of Mines and Geology (2006), Quaternary fault and fold database for the United States. [Available at http://earthquake.usgs.gov/hazards/qfaults/, accessed 15 Feb. 2014]

van Soest, M. C., K. V. Hodges, J. Wartho, M. B. Biren, B. D. Monteleone, J. Ramezani, J. G. Spray, and L. M. Thompson (2011), (U-Th)/He dating of terrestrial impact structures: The Manicouagan example, *Geochem. Geophys. Geosyst.*, *12*, Q0AA16, doi:10.1029/2010GC003465.

Wells, M. L., R. D. Dallmeyer, and R. W. Allmendinger (1990), Late Cretaceous extension in the hinterland of the Sevier thrust belt, northwestern Utah and southern Idaho, *Geology*, *18*(10), 929–933, doi:10.1130/0091-7613(1990)018<0929:LCEITH>2.3.CO;2.

Wells, M. L., L. W. Snee, and A. E. Blythe (2000), Dating of major normal fault systems using thermochronology: An example from the Raft River detachment, Basin and Range, western United States, *J. Geophys. Res.*, *105*(B7), 16,303–16,327, doi:10.1029/2000JB900094.

Wendt, I., and C. Carl (1991), The statistical distribution of the mean squared weighted deviation, *Chem. Geol.*, *86*(4), 275–285.

Wernicke, B. (1992), Cenozoic extensional tectonics of the US Cordillera, in *The Cordilleran Orogen: Conterminous U.S*, vol. G-3, edited by B. C. Burchfiel, P. W. Lipman, and M. L. Zoback, pp. 553–581, Geol. Soc. of Am., Boulder, Colo.

Wesnousky, S. G., and C. H. Willoughby (2003), Neotectonic note: The Ruby–East Humboldt Range, northeastern Nevada, *Bull. Seismol. Soc. Am.*, *93*(3), 1345–1354, doi:10.1785/0120020032.

Whitebread, D. H. (1969), Geologic map of the Wheeler Peak and Garrison quadrangles, Nevada and Utah, *U.S. Geol. Surv. Misc. Invest. Map 1–578*, 1:48,000 scale.

Whittington, A. G., A. M. Hofmeister, and P. I. Nábělek (2009), Temperature-dependent thermal diffusivity of the Earth's crust and implications for magmatism, *Nature*, *458*(7236), 319–321, doi:10.1038/nature07818.

Wolf, R., K. Farley, and L. Silver (1996), Helium diffusion and low-temperature thermochronometry of apatite, *Geochim. Cosmochim. Acta*, *60*(21), 4231–4240, doi:10.1016/S0016-7037(96)00192-5.

Wolf, R., K. Farley, and D. Kass (1998), Modeling of the temperature sensitivity of the apatite (U–Th)/He thermochronometer, *Chem. Geol.*, *148*(1), 105–114, doi:10.1016/S0009-2541(98)00024-2.

Wolfe, M. R., and D. F. Stockli (2010), Zircon (U–Th)/He thermochronometry in the KTB drill hole, Germany, and its implications for bulk He diffusion kinetics in zircon, *Earth Planet. Sci. Lett.*, *295*(1), 69–82, doi:10.1016/j.epsl.2010.03.025.